Geoscience Frontiers 17 (2026) 102279

Contents lists available at ScienceDirect

Geoscience Frontiers

journal homepage: www.elsevier.com/locate/gsf

Research Paper

Petrogenesis of tonalite-trondhjemite and potassic granite, Geita Greenstone Belt, Tanzania Craton: Implication for crustal evolution during Neoarchean plate tectonic initiation

I. Gamal-Adeen [a,*], M.G. Shahien [a], A.M. Zayed [a], B.R. Bakhit [a], I.V. Sanislav [b], A.S.A.A. Abu Sharib [c]

[a] *Faculty of Science, Beni-Suef University, Beni-Suef 62521, Egypt*
[b] *Economic Geology Research Centre (EGRU), College of Science and Engineering, James Cook University, Townsville, QLD 4811, Australia*
[c] *Faculty of Earth Sciences, Beni-Suef University, Beni-Suef 62521, Egypt*

ARTICLE INFO

Article history:
Received 17 June 2025
Revised 3 January 2026
Accepted 3 February 2026
Available online 7 February 2026

Keywords:
Geita Greenstone Belt
Neoarchean granitoids
Amphibolite facies
Partial melting
Flat subduction
Crustal delamination

ABSTRACT

Geochemical and zircon isotope data reveal a complex petrogenetic history of the Neoarchean granitoids of the Geita Greenstone Belt (GGB), northern Tanzania Craton. Geochemically, the granitoids are categorized into: (1) tonalite-low-silica trondhjemite; (2) high-silica trondhjemite; (3) transitional granitoids; and (4) potassic granite. Compared to tonalite-low-silica trondhjemite, the high-silica trondhjemite displays significant depletion in HREE and HFSE, and have an exceptional high Sr/Y and La_N/Yb_N ratios. Both categories display similar LREE and LILE patterns. Transitional granitoids comprise dykes and dyke-like bodies of low-silica trondhjemite and quartz monzonite. Characteristically, they have low La_N/Yb_N and Sr/Y ratios, and are strongly-enriched in LREE and LILE and less depleted in HREE and HFSE. Potassic granite is represented by small intrusions and dykes that exhibit low La_N/Yb_N and low to moderate Sr/Y ratios, and are moderately-enriched in LREE, strongly-enriched in LILE, and moderately-depleted in HREE and HFSE. The tonalite and low-silica trondhjemite generated (~2699–2714 Ma) by partial melting of basaltic rock at amphibolite facies metamorphic condition. The high-silica trondhjemite evolved from fractionation of the tonalitic melt. Lithospheric delamination produced high-K mafic magma that fractionated into the transitional granitoids (~2660–2683 Ma), and caused partial melting of the tonalite-trondhjemites to generate the potassic granite (~2646–2685 Ma). Geochemical signature of the tonalite-trondhjemites and potassic granite, as indicated by the negative Nb-Ta-Ti anomalies, and strongly-fractionated REEs, supported with the structural style near and at the contact between the felsic gneisses and the greenstone belt infer generation of the gneisses at a convergent plate boundary. Partial melting at the base of an oceanic plateau or a flat subducting slab has been suggested to interpret the evolution of the northern Tanzania Craton (2700–2650 Ma). A metasomatized mantle was introduced by lower crustal delamination/break-off of the down-going slab.

1. Introduction

The nuclei of continental masses are occupied by granite-greenstone/Archean terranes and cratons having limited surface exposures (Fig. 1) compared to the Proterozoic terranes. The Archean terranes consist of complexly deformed felsic gneisses, granites and greenstone belts. The gneisses are marked by amphibolite to granulite facies assemblages originated mostly from the melting of a mafic igneous source (Almeida et al., 2011, 2013), and are dominated by tonalite-trondhjemite-granodiorite (TTG) rocks reflecting an early crustal differentiation. The granites consist of late-tectonic high-K usually undeformed intrusions derived from melting of the TTG parental magma, and mark the stabilization of the craton (e.g. Mshiu and Maboko, 2012; Almeida et al., 2013; Laurent et al., 2014; Marimon et al., 2022). The greenstone belts are dominated by greenschist facies mafic volcanics and ultramafic rocks with subordinate felsic volcanics and volcano-metasedimentary successions. The gneisses and greenstone rocks are intruded by Neoarchean high-K granites (Moyen and Martin, 2012; Mshiu and Maboko, 2012; Laurent et al., 2014; Sanislav et al., 2014; Hastie et al., 2023).

---

* Corresponding author.
E-mail address: g_israa@science.bsu.edu.eg (I. Gamal-Adeen).

https://doi.org/10.1016/j.gsf.2026.102279

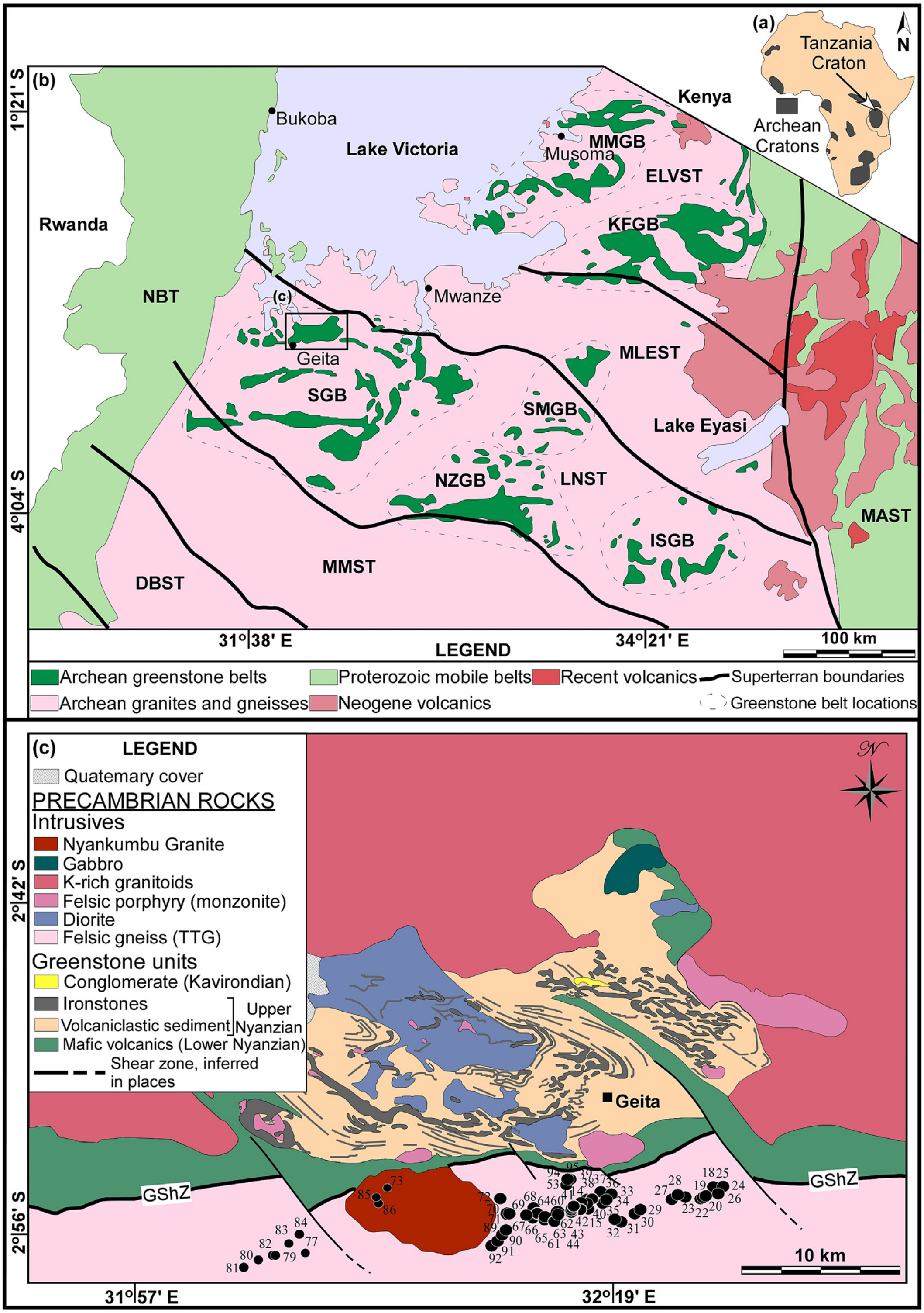

Fig. 1. (a) The distribution of Archean cratons in Africa. (b) A simplified geologic map of northern Tanzania Craton shows WNW–ESE-trending super-terranes exposing Archean granitic gneisses and greenstone belts (after Sanislav et al., 2018b). Greenstone Belts: Sukumaland (SGB); Nzega (NZGB), Shynianga-Malita (SMGB), Iramba-Sekenke (ISGB), Kilimafedha (KFGB), Musoma-Mara (MMGB); Super-Terranes: East Lake Victoria (ELVST), Mwanza Lake Eyasi (MLEST), Lake Nyanza (LNST), Moyowosi-Manyoni (MMST), Dodoma Basement (DBST), Mbulu-Masai (MAST), Nyakahura-Burigi (NBT). (c) The main lithostratigraphic units of Geita Greenstone Belt, inset (c) in (b), separated from the southern Archean gneiss by a major E–W-trending shear zone (GShZ), and intruded by a number of intrusives (after Sanislav et al., 2018b).

Archean granitoids have no modern-day analogues. Consequently, the genesis, mechanism and tectonic setting of the Archean TTGs have long been controversial (Smithies, 2000; Hawkesworth et al., 2010; Sanislav et al., 2014; Roberts et al., 2015). For instance, whether the TTGs were generated by fractional crystallization of a basaltic magma (Kamber et al., 2002; Kleinhanns et al., 2003; Martin and Sigmarsson, 2005; Jagoutz et al., 2013; Liou and Guo, 2019; Smithies et al., 2019) or partial melting of a crystalline mafic rock (Halla et al., 2009; Smithies et al., 2009; Almeida et al., 2011; Martin et al., 2014; Wu et al.,

2023) at orogenic (Martin et al., 2005, 2014; Manya, 2016; Marimon et al., 2022; Wu et al., 2023) or anorogenic/within plate (Whalen et al., 2002; Bédard, 2006; Smithies et al., 2009; Keller and Schoene, 2012) tectonic settings is debatable. Moreover, at a convergent plate boundary, the subduction style and metamorphic condition responsible for generating the TTG melt are controversial (Moyen and Martin, 2012). At amphibolite facies condition, the rocks are buoyant enough to favor shallow and flat subduction (Foley et al., 2002), and hence the melt is produced at relatively shallow crustal levels. On the other hand, with progressive eclogitization, the denser rocks formed would steepen the subducting slap, and hence the melt is produced at deeper crustal levels (Rapp et al., 2003; Condie, 2005). Furthermore, the geochemical diversity and heterogeneity of the Archean granitoids and TTGs composition, i.e., low- and high-HREE groups (Halla et al., 2009) deepen the controversy. Although Archean TTGs share common geochemical characteristics with modern-day adakites (Martin, 1999; Kamber et al., 2002; Martin and Moyen, 2002; Condie, 2005; Martin and Sigmarsson, 2005; Maboko et al., 2006; Martin et al., 2014; Ganade et al., 2017; Wu et al., 2023), significant differences in REE fractionation, Mg# values and SiO_2 contents (Martin, 1999; Smithies, 2000; Smithies et al., 2003) suggest a different tectonic process (Condie, 1997; Martin, 1999; Smithies, 2000; Smithies et al., 2003; Condie, 2005; Harris and Bédard, 2014; Ganade et al., 2017; Sanislav et al., 2018a).

The Geita Greenstone Belt (GGB; Fig. 1a–c), located in the northern part of the Archean Tanzania Craton, is dominated by mafic amphibolites intercalated with volcaniclastics and schists, and bounded to the south by a major E–W-trending shear zone (Cook et al., 2016; Sanislav et al., 2018b; Kwelwa et al., 2018a) that separates it from felsic gneisses of tonalitic and trondhjemitic composition. The greenstone belt is intruded by a series of *syn*-tectonic intermediate to felsic intrusive complexes (Sanislav et al., 2015; Kwelwa et al., 2018b). The northern, eastern and western margins of the greenstone belt are intruded by late tectonic high-K granites.

This contribution presents a detailed whole-rock geochemical investigation complemented with Lu-Hf isotope systematics in zircon grains of the TTGs and granites occupying the southern part of the greenstone belt, to decipher the genesis, formation, crustal growth and tectonic implications of the Archean granitoids.

2. Geologic setting

The Archean Tanzania Craton occupies the central and northern parts of Tanzania, western part of Kenya, and southeastern Uganda (Fig. 1a and b; Clifford, 1970). The northern part of the Craton, known as the Lake Victoria Region, is subdivided, into WNW–ESE trending super-terranes bounded by NW-trending shear zones (Kabete et al., 2012; Fig. 1b). From north to south, the super-terranes are: East Lake Victoria (ELVST), Mwanza Lake Eyasi (MLEST) and Lake Nyanza (LNST). They enclose nearly E–W-trending granitoids-greenstone belts: Musoma-Mara (MMGB), Kilimafedha (KGB), Sukumaland (SGB), Shinyanga-Malita (SMGB), Nzega (NGB) and Iramba-Sekenke (ISGB) (Borg and Shackleton, 1997; Kabete et al., 2012), that vary considerably in the stratigraphy, geochemical signature, age and tectonic evolution (Kwelwa et al., 2018a; and references therein). The lens-shaped greenstone belts, up to 30 km wide and up to several hundred km long (Sanislav et al., 2014), are interpreted to be originated in back-arc basin, island or continental arc, and oceanic plateaus tectonic settings (Manya and Maboko, 2003, 2008; Manya et al., 2007; Mtoro et al., 2009; Messo et al., 2012; Cook et al., 2016).

The Geita Greenstone Belt (GGB), located in the northern margin of the (SGB), the extreme northwestern part of the Lake Nyanza supper-terrane (Fig. 1c), is differentiated into two main tectonostratigraphic units: the Nyanzian supergroups, at the base, and the Kavirondian supergroups, at the top (Borg and Shackleton, 1997). The former supergroup is distinguished into Lower and Upper Nyanzian groups separated by a structural discontinuity (Cook et al., 2016). The lower group comprises mafic amphibolites with subordinate felsic metavolcanics and ultramafic rocks referred to as Kiziba Formation (Manya and Maboko, 2003; Cook et al., 2016). The upper group comprises greenschist facies volcaniclastics, turbidities and ironstones (Sanislav et al., 2015; Kwelwa et al., 2018b). The Kavirondian supergroup (2640–2790 Ma; Sanislav et al., 2018a) unconformably overlies the Nyanzian supergroup, and is composed of quartzite, grit and basal conglomerate (Gabert, 1990; Borg and Shackleton, 1997; Manya and Maboko, 2003; and references therein). To the north of the study area, the Nyanzian-Kavirondian supergroups are intruded by syn- and late-tectonic intrusives (Barth, 1990; Borg and Shackleton,1997; Manya and Maboko, 2003; Kabete et al., 2012; Sanislav et al., 2014). The southern margin of the GGB consists of a major, ~1 km-wide E–W-trending shear zone that separates Kiziba Formation to the north from coarse-grained felsic gneisses to the south (Fig. 1c; Sanislav et al., 2018b). The gneisses are marked by a strong SL fabric that extends for ~0.5 km, and represented by steeply dipping E–W-trending mylonitic foliation with pronounced E–W-trending sub-horizontal stretched mineral lineations. Southwards, away from the contact, the SL fabric decreases in intensity. At a distance greater than ~1 km, the gneisses show no sign of stretched lineations. The gneisses and the southern part of the Kibiza Formation are intruded by undeformed xenolithic Nyankumbu granite (Fig. 3j; Sanislav et al., 2018b). The xenoliths, a few to tens of centimeters across, have composition similar to that of the gneisses. In high strain zones, the gneisses are dissected by dyke-like to lensoidal bodies of granite and granodiorite composition preserving an SL fabric consistent with that of the gneisses (Fig. 3b, h and i; Sanislav et al., 2018b).

3. Methodology

Representative samples were milled, in a tungsten carbide ring mill and analyzed at the Advanced Analytical Centre at James Cook University (JCU). Major elements were determined by X-ray fluorescence (XRF) spectroscopy using a Bruker-AXS, S4 Pioneer XRF Spectrometer. Trace elements analyses were conducted via inductively coupled plasma mass spectrometry (ICP-MS) using a Varian ICP-MS 820 spectrometer. For zircon chemistry, representative samples were milled, in a tungsten carbide disk mill, and sieved to <500 μm. The fraction <500 μm was run through a Frantz magnetic separator. Zircon grains were separated from the non-magnetic fraction, mounted in epoxy resin and polished. The grains were examined by a Jeol JSM5410LV with attached cathodoluminescence detector, and dated by LA-ICP MS. Zircon Hf–Lu ages and trace-element data were acquired by LA-ICP-MS. Hafnium isotopic compositions were measured on a Thermo-Scientific Neptune multi-collector ICP-MS attached to a Coherent GeoLas 193 nm ArF laser with 60 m laser beam diameters at a repetition rate of 4 Hz. The analytical procedures are detailed in Sanislav et al. (2014).

4. Results

4.1. Whole-rock geochemistry

The major and trace elements of 57 representative samples are listed in Supplementary Data 1, Table S1. According to O'Connor

(1965) discrimination diagram (Fig. 2a), the samples are discriminated into trondhjemites (41 samples) tonalites (4 samples) and granites (12 samples).

4.1.1. Tonalite-trondhjemites

The tonalite-trondhjemites samples are characterized by variable SiO_2 (63.9–74.4 wt.%) content, high Na_2O (4.5–7.2 wt.%) and Al_2O_3 (14.4–17.8 wt.%) contents, low TiO_2 (0.10–0.41 wt.%), MgO (0.17–1.05 wt.%), CaO (1.2–3.8 wt.%), P_2O_5 (0.03–0.12 wt.%) and K_2O (0.61–3.5 wt.%) contents, and by low Mg# ($Mg^{2+}/(Mg^{2+}+Fe^{2+})$ = 12–53) value (Supplementary Data 1, Table S1). The low K_2O content accounts for the low K_2O/Na_2O (0.08–0.76 wt.%) ratio (Supplementary Data 1, Table S1).

In terms of silica, total alkali and calcium contents, the trondhjemite can be loosely distinguished into two subvarieties: high-silica (71.1–74.4 wt.%) and low-silica (63.9–72.6 wt.%) trondhjemites. At the mesoscopic scale, high-silica trondhjemite occurs mainly near the metavolcanic contact. The low-silica trondhjemite together with the tonalite represents the main mass of the felsic gneisses. A few small intrusions of low-silica trondhjemite have been recorded as dykes cutting across the felsic gneisses. The two sub-varieties of low-silica trondhjemites are further distinguished by their (FeO^T + MgO + MnO + TiO_2), and K_2O and Na_2O contents (Supplementary Data 1, Table S1). A sample with a very low-silica (SM34; SiO_2 = 63.9 wt.%) content is identified as quartz monzonite using TAS diagram of (Middlemost, 1985; Fig. 2b).

On granite discrimination diagrams (Frost et al., 2001), the majority of tonalite-trondhjemites samples are calcic to calc-alkalic (Fig. 2c). Based on the molar alkalis, aluminum, and calcium, the samples show low A/CNK ratio. In terms of the aluminum saturation index (ASI), they range from 0.87 to 1.05 indicative of a slightly peraluminous to metaluminous character (Fig. 2d). On the Harker diagrams, Al_2O_3, FeO^T, MgO, TiO_2, P_2O_5, CaO, and Na_2O display a negative correlation with SiO_2 (Fig. 3a–i), whereas K_2O, (Na_2O + K_2O) and K_2O/Na_2O ratio positively correlate with SiO_2 (Fig. 3j–l). The low-silica trondhjemites and tonalites display an overlap in the FeO^T, MgO, TiO_2 and P_2O_5 contents, whereas the high-silica trondhjemite overlaps with potassic granite in the latter values (Fig. 3b–f). Major elements geochemistry of the tonalite-trondhjemites demonstrates a typical characteristic of the Archean TTG (Fig. 4a and b; e.g. Martin et al., 2005; Huang et al., 2013; Laurent et al., 2014; and references therein). On the Na_2O-K_2O-CaO ternary diagram of Moyen et al. (2003), samples of the main gneissic trondhjemites and tonalites are restricted to the TTG field, whereas the low-silica (dyke-like) trondhjemites and quartz monzonite belong to the sanukitoids and enriched TTG field (Fig. 4a). The high-silica trondhjemites occupy the TTG and sanukitoids and enriched TTG fields (Fig. 4a). The dyke-like low-silica trondhjemite and quartz monzonite have higher SiO_2 and lower FeO^T + MgO contents and lower Mg# value relative to the sanikitoids (e.g., Laurent et al., 2014; Sun et al., 2020). Accordingly, they fit into the enriched TTG category of Laurent et al.

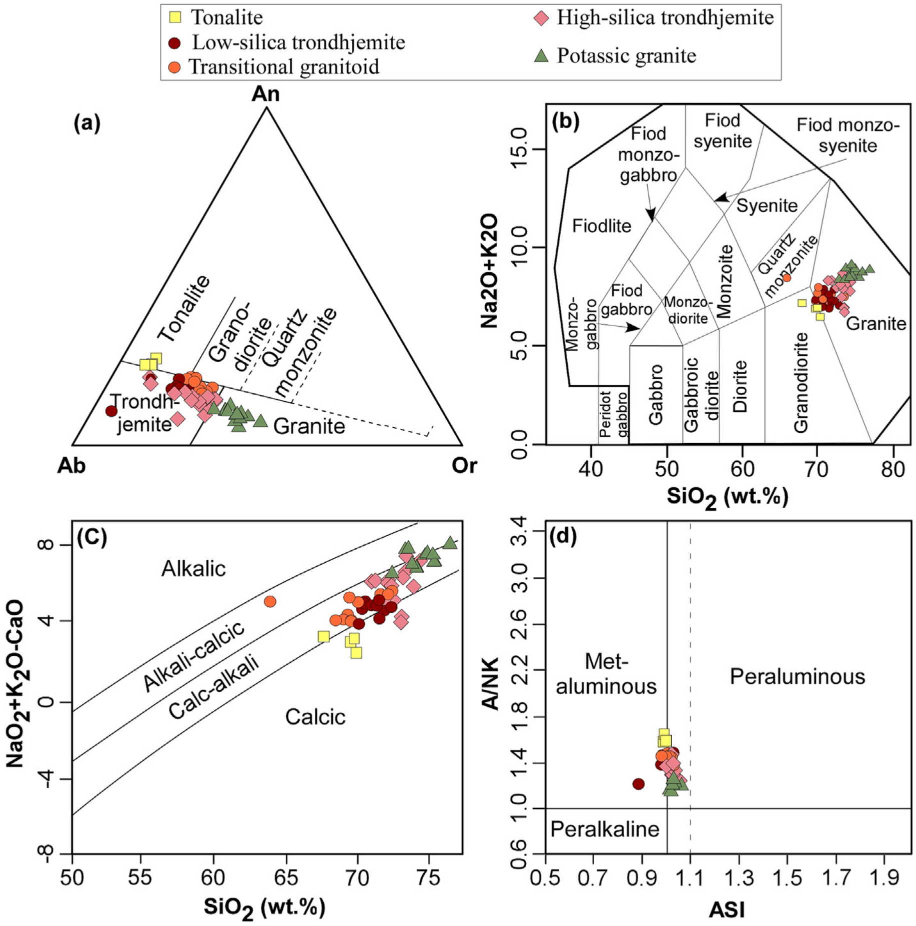

Fig. 2. (a) Normative Ab-An-Or classification diagram of O'Connor (1965) (modified by Baker, 1979) displays the different varieties of Geita granitoid. (b) Total alkalis vs. silica (TAS) diagram after Middlemost (1985) shows the classification of Neorchean Geita granitoids. Binary diagrams (after Frost et al., 2001) show (c) modified the alkali-lime index (MALI) and (d) alumina saturation index of the TTs and potassic granite. A/NK: molar $[Al_2O_3/(Na_2O + K_2O)]$; ASI (aluminum saturation index): molar $[Al_2O_3/(CaO + Na_2O + K_2O)]$.

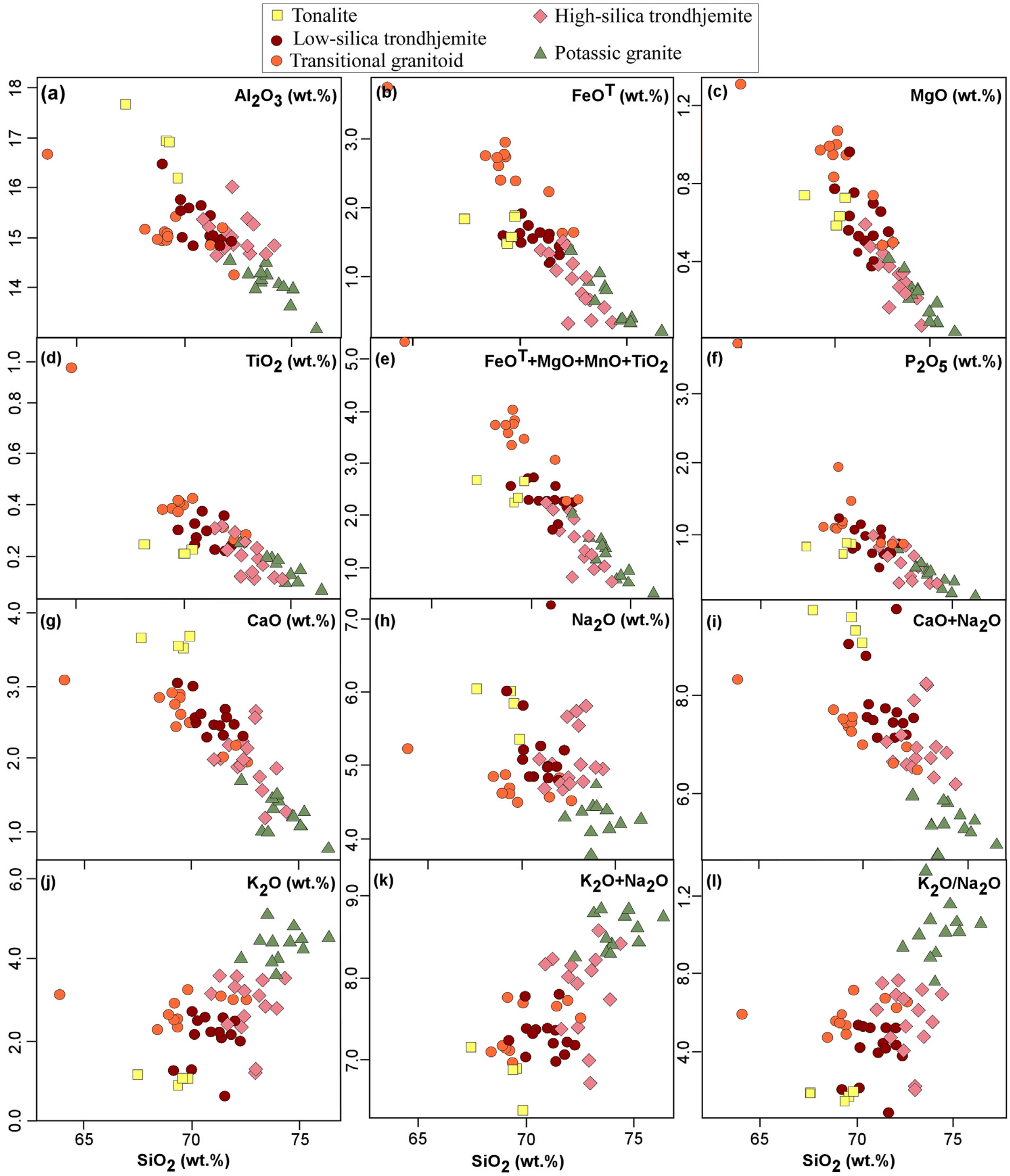

Fig. 3. (a–l) Harker variation diagrams of selected major elements vs. SiO_2 for the TTs, low-silica trondhjemite (TRANG) and potassic granite.

(2014), and equivalent to the transitional TTG (e.g., Moyen, 2011). The dyke-like low-silica trondhjemite and quartz monzonite (transitional granitoid) are denoted as TRANG, and the tonalite-trondhjemites as TTs (e.g., Marimon et al., 2022). Moreover, on the basis of Al_2O_3 and SiO_2 contents, the majority of Geita TTs and TRANG belong to the high-Al_2O_3 group of the TTGs of Baker (1979).

On the chondrite- and primitive mantle-normalized trace element diagrams (Anders and Grevesse, 1989; Sun and McDonough, 1989), the TTs are enriched in LREEs and LILEs relative to HREEs and HFSEs, respectively (Figs. 5a–c and 6a–c). The chondrite-normalized REE diagrams display moderately fractionated LREE pattern and slight inclination for HREE reflected by the ratios of La_N/Sm_N (2.0–9.9) and Gd_N/Yb_N (1.4–6.3), respectively (Fig. 5a–c). The TTs and TRAN.G exhibit a wide range of the La_N/Yb_N ratios (7.8–159) and Sr/Y (25.5–333.09) ratios coupled with the low contents of Yb_N (0.98–8.57 ppm) and Y (2.27–16.79 ppm), respectively (Fig. 7a and b). Together with the strong depletion of HREEs, the high-silica trondhjemite demonstrates higher ratios of La_N/Yb_N (21–114.8) relative to the tonalites (La_N/Yb_N 8–19.2). The majority of TTs and TRANG samples are characterized by moderately negative to no Eu anomalies

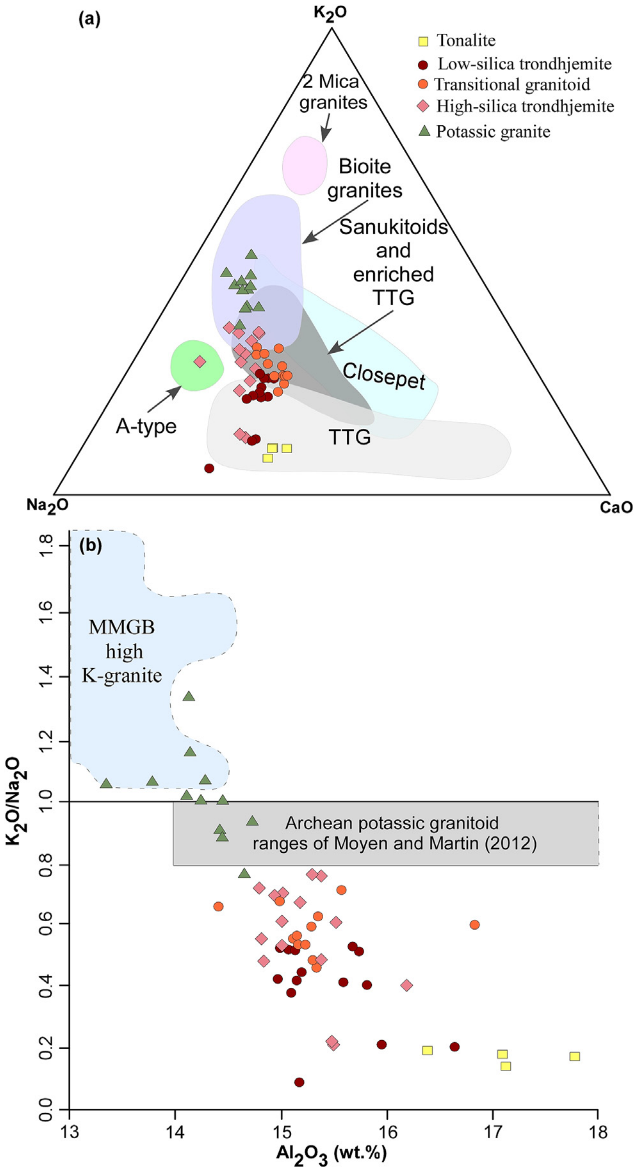

Fig. 4. (a) Na_2O-K_2O-CaO ternary diagram of Moyen et al. (2003). The tonalite and low-silica trondhjemite (the main gneissic mass), and low-silica trondhjemite (TRANG) occupy the TTG and sanukitoids and enriched TTG fields, respectively. (For more details, see field description). High-silica trondhjemite plots in both the TTG and sanukitoids and enriched TTG fields. Potassic granite plots within the biotite granite field. (b) Geita granitoids plots within the K_2O/Na_2O vs. Al_2O_3 diagram. The potassic granite overlap with the high K-granite of Mshiu and Maboko (2012; light blue field) from Musoma-Mara Greenstone Belt (MMGB), northern Tanzania Craton; and with the Archean potassic granite range of Moyen and Martin (2012; grey field).

(Eu/Eu*= 0.62–1.08). Five outliers of TTs and a TRANG sample have slightly positive Eu anomalies (Eu/Eu*=1.10–1.44). The Eu anomalies show no correlation with (Na_2O + CaO) or K_2O contents, except for the TRANG samples (Fig. 8a and b), and display strong correlation with Sr/Y ratio particularly for the high-silica trondhjemite (Fig. 8c). On the multi-elements spidergram, the TTs and TRANG samples display strong positive Pb-U anomalies and negative Nb-Ti-P anomalies (Fig. 6a–c). Compared to the TTs that have consistent positive Sr anomalies ($Sr/Sr^* = Sr_N/[(Pr_N + Nd_N)/2]$) = 1.16–11.68), the TRANG has anomalies that range from strong negative to slightly positive (Sr/Sr*= 0.64–1.84). The TTs and TRANG have low K/Rb (98–459), Nb/Ta (1.4–9.5) and Nb/La (0.065–0.539) ratios, and high Zr/Sm (18.3–91.5) and Sr/Y (25.5–333.09) ratios (e.g. Foley et al., 2002; Condie, 2005; Maboko et al., 2006; Laurent et al., 2014). Compared to the trace elements averages of the upper continental crust of Rudnick and Gao (2014), the TTs and TRANG samples have similar Th (1.2–17.6 ppm; Av. = 8.7 ppm) and U (0.45–7.44 ppm; Av. = 2.6 ppm) values, and lower Cr (9.25–45.57 ppm; Av. = 26 ppm) and V (38.23–94.33 ppm; Av. = 56.5 ppm) contents. The results show that, except for the relatively low MgO (and Mg#) and Cr contents, and slightly higher SiO_2 content (e.g. Smithies, 2000; Foley et al., 2002; Martin et al., 2005, 2014), the Neoarchean Geita TTs and TRANG share geochemical characteristics that are consistent with the modern high silica adakites (HSA).

4.1.2. Potassic granites

Granite samples, compared to the tonalites-trondhjemites, have higher SiO_2 (73.3–76.5 wt.%; Av. = 74.46 wt.%), and K_2O (3.57–5.04 wt.%) contents, lower Na_2O (3.78–4.73 wt.%), Al_2O_3 (13.3–14.7 wt.%), MgO (0.03–0.42 wt.%), Mg# (6.89–12.13), CaO (0.74–1.71 wt.%) and P_2O_5 (0.01–0.08 wt.%) contents, higher K_2O/Na_2O (0.75–1.33) ratio, and similar TiO_2 (0.06–0.25 wt.%) contents (Fig. 3a–l). The granite is calc-alkali to alkali-calcic, and weakly peraluminous, with ASI that ranges from 1.00 to 1.05 (Fig. 2c and d).

Akin to the TTs and TRANG, the potassic granite has low contents of Cr (19–31.2) and V (32.69–54.08). It is depleted in the HREEs and HFSEs (Nb, P, Ti, Zr and Y) and enriched in the LREEs and LILEs (Figs. 5d and 6d). The potassic granite and TTs share a common trace element pattern (Fig. 5c and d). However, although the granite and the TTs show a considerable overlap in the majority of the REEs, the granite is slightly enriched in LREEs (Rb, K and Pb) and a slightly depleted in HREEs relative to the TTs (Fig. 5a and d). Moreover, the granite has a slightly lower La_N/Yb_N (7.2–56.4), La_N/Sm_N (2.67–7.09) and Gd_N/Yb_N (1.22–3.86) ratios (Fig. 5d; Supplementary Data 1, Table S1).

Moreover, the granite generally has a moderately negative Eu (Eu/Eu*= 0.71–0.93) anomaly except one sample that shows a strong negative anomaly (0.47 in one sample), and three outlier samples with no Eu anomalies (Eu/Eu* = 1.04–1.07). The primitive mantle-normalized pattern displays strong enrichment in the LILEs (Rb, K and Pb), and heavy depletion in Sr, P and Ti relative to those of the TTs (Fig. 6d). It also displays a negative Nb anomaly, and slightly negative to slightly positive Sr anomalies (Sr/Sr* = 0.995–2.12). The granite has low K/Rb (179–326), Nb/Ta (1.8–5.5) and Nb/La (0.106–0.806) ratios, and high Zr/Sm (30.7–62.2), and Sr/Y (20.97–174.2) ratios. Compared to the TTs, the latter ratio is relatively low whereas that of the Th/Nb (1.37–6.79) is higher. According to the Neoarchean granitoids' classification of Moyen et al. (2003) and Laurent et al. (2014), the granite belongs to the biotite-bearing granites that are equivalent to the potassic granites of Moyen (2011) and Moyen and Martin (2012) (Fig. 4a and c).

4.2. Zircon trace elements and Lu–Hf isotopic compositions

Six samples from the tonalite (TTs), trondhjemite (TRANG), and potassic granite are analyzed for zircon trace elements, and Lu-Hf isotopic composition. Fourteen chemical analyses from one tonalite (SM02), and one potassic granite (SM01) samples, and thirty-two Lu–Hf isotopic compositions from two tonalite (SM02 and SM25), one trondhjemite (TRANG; SM07), and two potassic granite (SM23 and SM27) samples are listed in Tables 1 and 2, respectively. $^{207}Pb/^{206}Pb$ zircon data (Table 2) is presented in Sanislav et al. (2018b). Zircon temperature, based on Ti content of zircon, is estimated by the equation of Watson et al. (2006):

$$T_{\text{zircon}}\,(^{\circ}\text{C}) = \frac{5080\pm30}{(6.01\pm0.03)-\log(\text{Ti})} - 273 \text{ (Table 1).}$$

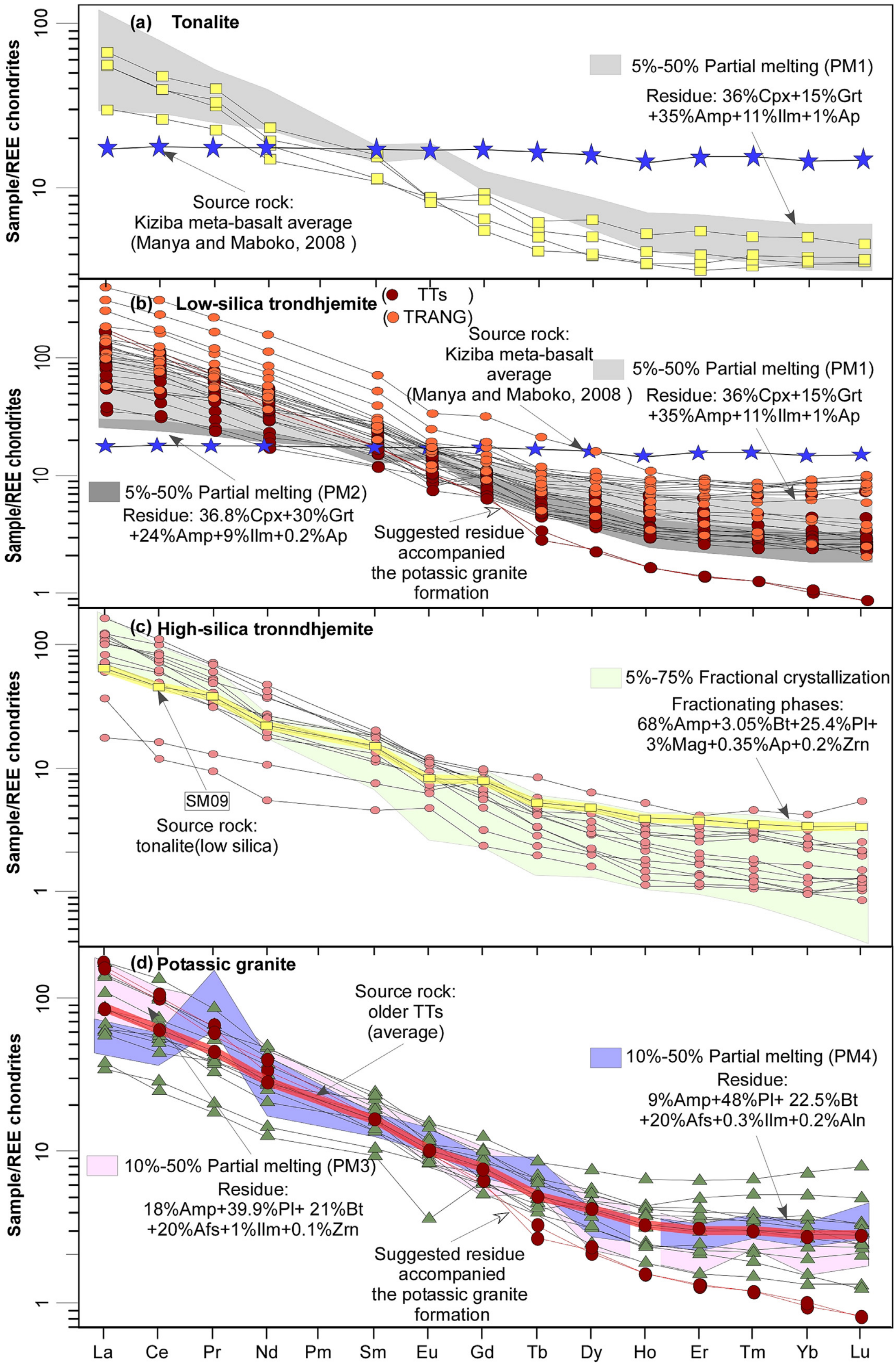

Fig. 5. (a–d) Chondrite normalized REE diagram for Geita TTs, TRANG and potassic granite. Two proposed equilibrium melting models (a, b and d) and Rayleigh fractionation model (c) to match the suggested source rocks. Chondrite values from Anders and Grevesse (1989). Afs: Alkali feldspar; Aln: Allanite; Amp: Amphibole; Ap: apatite; Bt: biotite; Cpx: Clinopyroxene; Grt: Garnet; Hb: hornblende; Ilm: Ilmenite; Pl: plagioclase; Mag, magnetite; Tit: titanite; Zrn, zircon (Whitney and Evan, 2010).

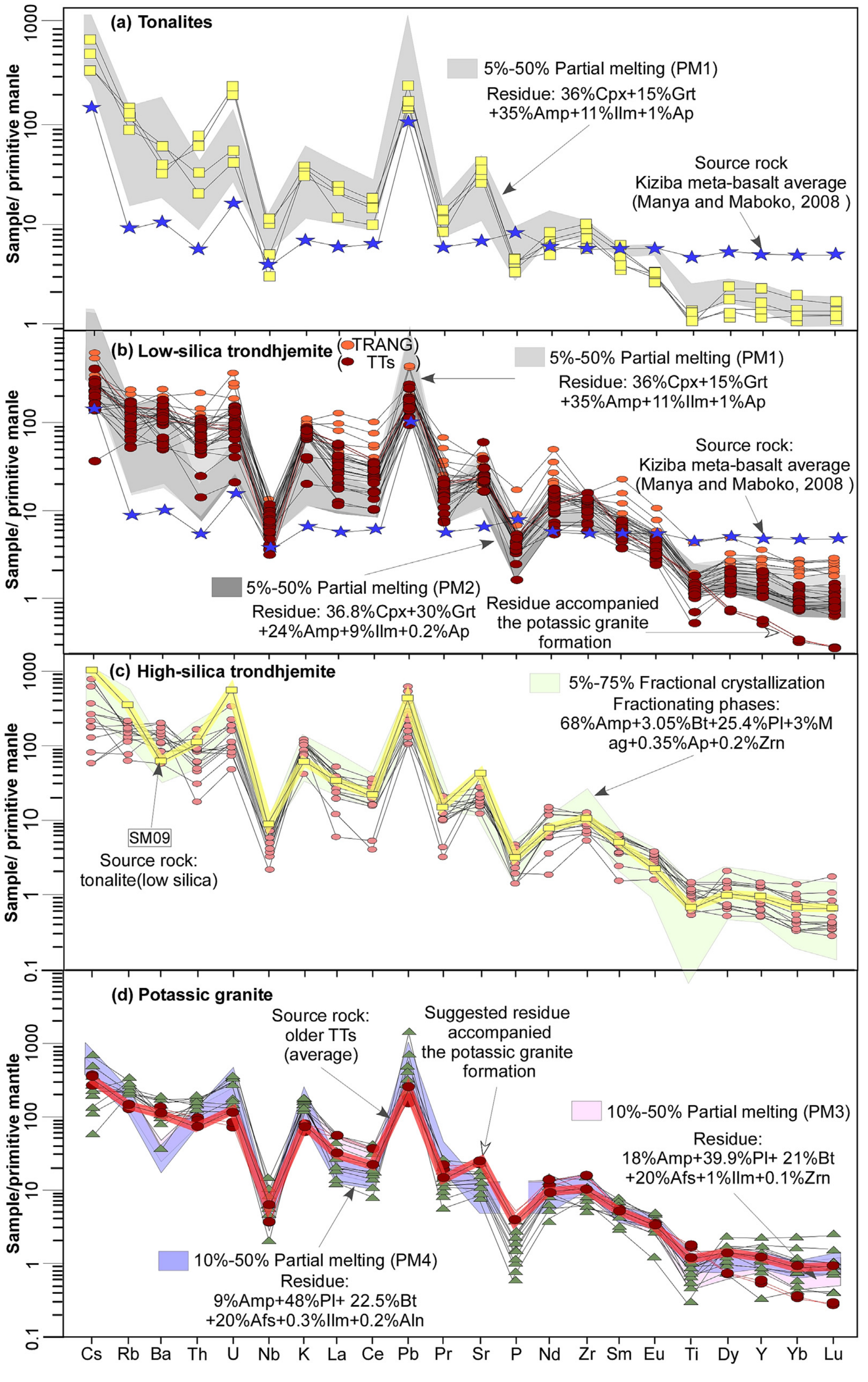

Fig. 6. (a–d) Primitive mantle normalized multi-elements spidergrams for Geita TTs, TRANG and potassic granite. Two equilibrium melting models and Rayleigh fractionation model attempting to match the suggested source rocks. Primitive mantle values from Sun and McDonough (1989). Afs: Alkali feldspar; Aln: Allanite; Amp: Amphibole; Ap: apatite; Bt: biotite; Cpx: Clinopyroxene; Grt: Garnet; Ilm: Ilmenite; Pl: plagioclase; Mag, magnetite; Tit: titanite; Zrn, zircon (Whitney and Evan, 2010). (Note: The strong Ti depletion in model (c) relative to that of Geita is attributed to the estimated calcic amphibole (after Bédard, 2006) rather than the residual low Mg# amphibole).

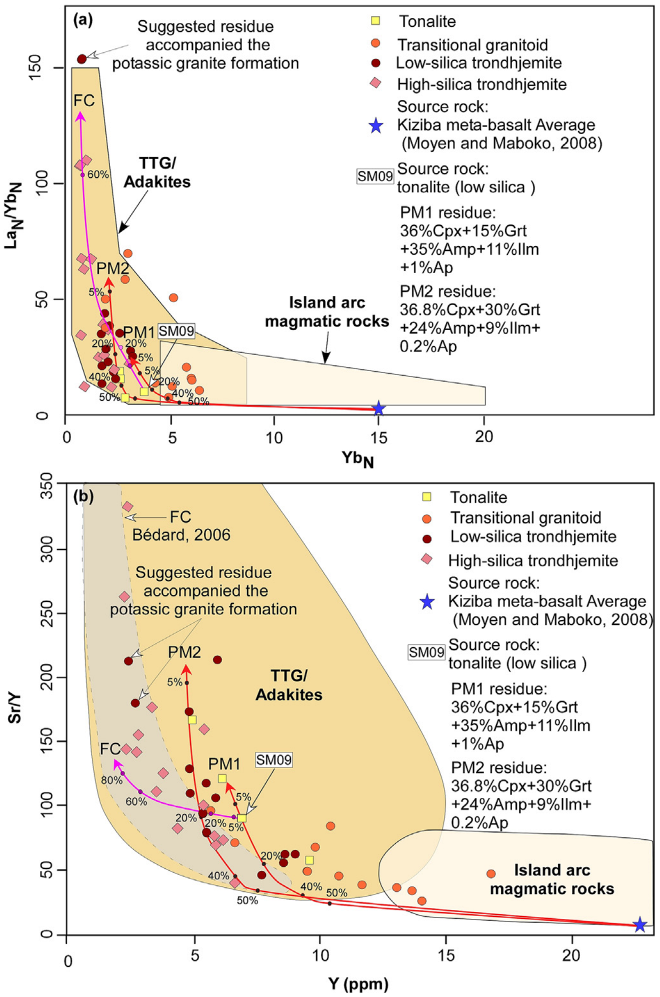

Fig. 7. TTs and TRANG plots on the La$_N$/Yb$_N$ vs. Yb$_N$ (a) and Sr/Y vs. Y (b) diagrams (after Martin et al., 2005; Drummond and Defant, 1990, respectively). The majority of the TTs and TRANG belong to the TTG field whereas a few TRANG samples plot within the island arc field. The red and pink curves represent the partial melting (PM1 and PM2) and fractionation (FC) paths of Kiziba mafic source (blue star) and parental tonalitic melt (yellow square; SM09), respectively. The grey field in (b) shows the outline of trondhjemite samples from Minto Block, NE Superior Province (Bédard, 2006). Outliers of low-silica trondhjemite are most probably the remains left after the melting of TTs that generated potassic granite. Amp: Amphibole; Ap: apatite; Cpx: Clinopyroxene; Grt: Garnet; Ilm: Ilmenite (Whitney and Evan, 2010).

4.2.1. Tonalite-trondhjemites

Zircon from tonalites (TTs) are represented by sub- to euhedral elongated crystals, most of which display a weakly-developed oscillatory zoning (Fig. 9a–d) with bright outermost discontinuous rims (Fig. 9a and d). A few mostly subhedral and relatively short, zoned crystals are recorded (Fig. 9c). In a few crystals, less luminescent unzoned cores with resorbed grain edges (e.g., Olierook et al., 2020) are overgrown by oscillatory-zoned rims (Fig. 9e). Zircons from trondhjemite (TRANG) are sub- to euhedral elongated to equant oscillatory-zoned crystals (Fig. 9c). One zircon grain has a weakly luminescent unzoned core mantled by a well-developed growth zoning (Fig. 9e). Brighter unzoned metamorphic zircons have been recorded in a few samples (e.g. Corfu et al., 2003). Based on ^{207}Pb/^{206}Pb zircon ages, Sanislav et al. (2018b) recorded inherited Meso-Archean cores overgrown by Neoarchean rims from tonalite and trondhjemite samples (Fig. 9c and e).

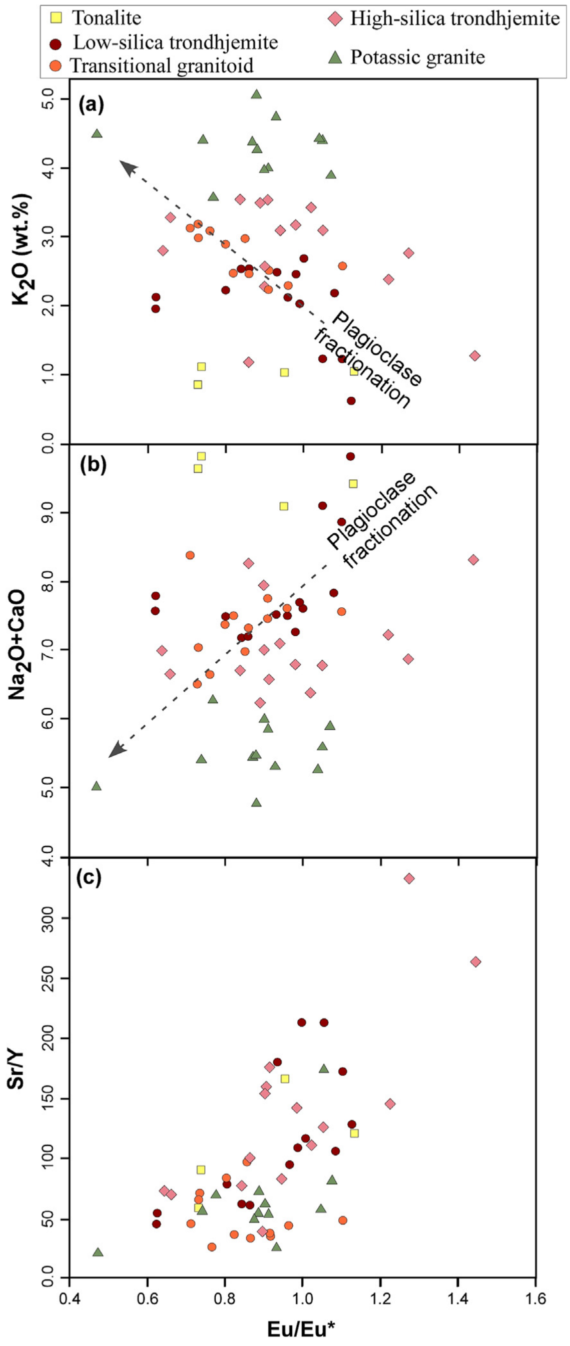

Fig. 8. (a–c) K$_2$O, (Na$_2$O + CaO) and Sr/Y vs. Eu anomalies (Eu/Eu*) variation diagrams of Geita granitoids. Transitional granitoid (TRANG) plots exhibit marked negative K$_2$O (a) and positive (Na$_2$O + CaO) (b) correlations with Eu/Eu*. The Eu anomalies vary independently with (Na$_2$O + CaO) and K$_2$O for the other varieties of Geita granitoids. (c) High silica trondhjemite displays a strong positive correlation of Sr/Y with Eu anomalies.

Trace element analyses of zircons (spots 1–8; Fig. 9a and b), from the tonalite (TTs) show low Th (7.5–102 ppm) and high U (401.4–682.15 ppm) contents with moderate (0.12–1.02 ppm) Th/U ratios, except for two crystals (spots 1, 5 and 6; Fig. 9a and b) that have low ratios (0.01–0.05). The low Th/U ratio (<0.07) is a distinctive criterion for metamorphic zircons, whereas oscillatory zoned crystals with higher Th/U ratio are indicative of magmatic zircons (e.g., Rubatto, 2002; Wu et al., 2009). An outlier (spot 4; Fig. 9a), has exceptionally high Th (1485.3 ppm) and U (1457.6 ppm) contents, and moderate Th/U ratio. The chondrite-normalized REE diagram (Fig. 10a) displays enriched HREE patterns relative to the LREEs (La$_N$/Yb$_N$ = 0.04–0.18) with negative to no Eu anomalies (Eu/Eu*= 0.69–1.09). A slightly positive Eu

Table 1
Trace element data for zircons from Geita tonalite and potassic granite. n.d.: not detected.

Element/ Sample	Tonalite								Potassic granite					
	SM02-1	SM02-2	SM02-3	SM02-4	SM02-5	SM02-6	SM02-7	SM02-8	SM01-1	SM01-2	SM01-3	SM01-4	SM01-5	SM01-6
Sr	34.45	36.06	81.73	166.97	62.12	47.44	51.22	19.48	162.28	472.39	284.39	24.17	47.5	484.13
Y	1211.94	1359.39	1162.73	6009	564.12	876.21	888.86	937.66	1413.02	3688.17	1730.31	382.99	779.62	2480.42
Nb	2.72	4.2	5.53	10.02	2.115	3.15	2.64	3.41	5.77	29.79	10.32	1.408	2.91	22.25
Sn	24.56	26.02	32.4	78.26	39.03	25.91	31.32	22.27	93.66	312.06	148.84	23.07	36.02	304.26
Sb	0.79	0.58	1.16	2.41	1.19	0.78	0.82	0.33	0.77	3.31	1.53	0.38	2.02	3.36
La	19.16	25.4	89.81	100.97	25.71	38.68	33.44	18.24	126.67	3194.56	753.84	28.19	126.24	61.54
Ce	85.75	139.82	349.54	388.97	91.64	173.58	199.24	106.67	746.44	13724.75	3019.7	37.94	558.37	117.11
Pr	16.65	25.36	59.45	53.12	16.65	32.28	37.11	21.52	64	1418.26	384.49	11.94	69.74	9.24
Nd	123.09	208.93	456.6	341	120.68	259.45	318.26	174.58	253.98	5741.6	1663.21	47.97	332.1	38.9
Sm	33.57	81.39	140.25	107.81	33.58	76.64	129.06	61.72	60.53	1122.63	263.2	15.91	56.56	22.91
Eu	10.66	22.52	41.97	34.35	15.2	25.7	30.03	12.57	15.99	323.63	61.86	5.16	20.62	14.76
Gd	39.13	91.83	138.74	211.95	36.65	66.76	111.34	n.d	82.76	n.d.	227.63	29.63	53.18	95.7
Tb	7.35	12.24	13.31	45.63	4.65	7.56	10.41	8.18	18.87	94.18	31.47	6.08	9.71	27.57
Dy	135.9	207.72	233.73	736.77	78.67	132.55	183.54	137.65	258.49	1308.86	444.24	80.36	138.84	386.39
Ho	35.7	40.18	32.9	179.38	15.93	24.74	26.64	27.22	47.39	114.22	54.91	12.83	24.36	78.05
Er	175.29	197.14	155.33	835.5	88.55	129.13	136.26	138.46	184.17	379.45	195.39	46.3	102.7	311.27
Tm	36.69	43.84	34.78	175.26	22.21	30.58	32.08	31.68	33.93	67.46	35.18	7.95	20.55	59.75
Yb	337.01	424.43	336.47	1629.53	250.43	318.36	332.31	321.97	277.85	551.64	288.82	62.67	182.37	503.31
Lu	70.15	92.54	71.02	331.83	61.02	72.18	77.9	70.72	48.56	90.11	48.14	11.46	35.65	85.22
Hf	18,191.64	19,897.83	24,066.53	15,949.7	23,419.18	24,228.97	20,920.96	22,370.62	18,144.76	25,459.25	22,313.07	14,465.92	18,264.41	25,042.89
Bi	0.14	0.02	0.05	0.19	0.02	0.1	0.03	0.02	0.07	1.39	0.26	0.07	0.11	1.12
Th	22.37	95.43	66.31	1485.31	7.52	24.08	102	65.55	434.18	2024.91	945.21	225.42	135.07	1997.23
U	432.14	461.33	549.36	1457.58	682.15	466.63	571.98	401.4	1888.26	5185.19	3075.33	404.43	669.86	6181.77
T_{zircon} (°C)	813.1	865.6	939	1066.5	817.8	818	780.2	819.5	845.2	1225.2	924.7	820.3	941.2	767.1
2σ ±	12	12	10.5	12	12	12	12	12	12	15	10.5	12	10.5	12.5

Table 2
Lu–Hf isotopic compositions of zircons from Geita tonalite (TTs), low-silica trondhjemite (TRANG) and potassic granite. $^{207}Pb/^{206}Pb$ zircon ages are obtained by Sanislav et al. (2018b).

Sample	Spot	$^{176}Lu/^{177}Hf$	±	$^{176}Hf/^{177}Hf$	±	$^{207}Pb/^{206}Pb$ age (Ma)	Initial $^{176}Hf/^{177}Hf$	$\varepsilon_{Hf}(0)$	$\varepsilon_{Hf}(t)$	±	T_{DM} (Ma)
Tonalite	SM02-01	0.00129	1.20E-04	0.281135	5.59E-06	2700	0.28107	−58.3587	0.72153	0.19873	2969.06
	SM02-04	0.00114	3.02E-05	0.28114	5.20E-06	2704	0.28108	−58.18	1.2604	0.18485	2950.86
	SM02-08	0.00066	3.58E-05	0.281092	6.90E-06	2709	0.28106	−59.8865	0.54319	0.24548	2979.17
	SM02-09	0.00139	7.40E-06	0.281136	7.37E-06	2714	0.28106	−58.3229	0.88863	0.26211	2975.48
	SM02-10	0.00134	2.92E-05	0.281101	1.19E-05	2699	0.28103	−59.5355	−0.58495	0.42307	3018.77
	SM02-12	0.00101	4.15E-05	0.281091	7.83E-06	2703	0.28104	−59.922	−0.26313	0.27851	3007.12
	SM25-03	0.00173	1.15E-05	0.281174	7.72E-06	2712	0.28108	−56.9859	1.55264	0.2746	2950.4
	SM25-06	0.00086	4.70E-06	0.281127	6.28E-06	2700	0.28108	−58.6286	1.24325	0.2234	2946.2
	SM25-08	0.00146	1.23E-05	0.281149	7.46E-06	2655	0.28107	−57.858	−0.10562	0.26521	2963.28
	SM25-12	0.00135	2.80E-06	0.281132	6.65E-06	2665	0.28106	−58.462	−0.2793	0.23669	2977.66
	SM25-13	0.00105	5.15E-05	0.281128	7.49E-06	2705	0.28107	−58.5927	1.02859	0.26635	2960.01
	SM25-17	0.00113	3.12E-05	0.281142	6.19E-06	2710	0.28108	−58.1379	1.49514	0.22013	2947.02
	SM25-19	0.0014	4.07E-05	0.281127	7.07E-06	2707	0.28105	−58.6447	0.38186	0.2516	2989.01
	SM25-20	0.00101	1.77E-05	0.28114	7.16E-06	2706	0.28109	−58.1873	1.53433	0.2545	2941.32
Transitional granitoid	SM07-05	0.0005	2.19E-05	0.281103	8.31E-06	2666	0.28108	−59.4842	0.25141	0.29566	2951.61
	SM07-06	0.00044	3.04E-05	0.281078	8.38E-06	2664	0.28106	−60.3672	−0.57049	0.29826	2980.24
	SM07-07	0.00119	1.97E-05	0.28112	1.18E-05	2666	0.28106	−58.8726	−0.38537	0.42117	2981.26
	SM07-08	0.0004	1.98E-05	0.281106	9.12E-06	2683	0.28108	−59.3889	0.91713	0.3244	2940.7
	SM07-09	0.00031	0.000413	0.281081	7.29E-06	2660	0.28106	−60.278	−0.34161	0.25929	2967.19
	SM07-15	0.00051	1.20E-05	0.28108	2.01E-05	2671	0.28105	−60.3386	−0.47124	0.71681	2983.17
Potassic granite	SM23-02	0.00043	1.02E-05	0.281101	6.97E-06	2646	0.28108	−59.554	−0.15759	0.24787	2949.07
	SM23-05	0.00074	7.09E-06	0.281109	1.03E-05	2676	0.28107	−59.2838	0.23955	0.36753	2962.58
	SM23-06	0.00065	6.71E-06	0.2811	7.95E-06	2671	0.28107	−59.576	0.00376	0.28268	2966.42
	SM23-08	0.00051	2.56E-05	0.281097	7.97E-06	2669	0.28107	−59.6911	0.09355	0.28368	2960.23
	SM23-15	0.00166	6.82E-05	0.281162	9.46E-06	2665	0.28108	−57.3872	0.22497	0.33653	2960.79
	SM23-18	0.00054	7.32E-06	0.281101	6.93E-06	2678	0.28107	−59.5476	0.38598	0.24656	2957.29
	SM27-07	0.00044	9.07E-06	0.281073	8.50E-06	2671	0.28105	−60.5243	−0.56327	0.30247	2986.04
	SM27-10	0.00068	1.30E-05	0.281078	2.98E-05	2680	0.28104	−60.3643	−0.62984	1.06039	2998.34
	SM27-11	0.00096	4.83E-06	0.281086	1.15E-05	2685	0.28104	−60.096	−0.76561	0.4078	3010.25
	SM27-12	0.00018	2.50E-05	0.281069	8.02E-06	2680	0.28106	−60.6775	−0.03699	0.28549	2972.13
	SM27-14	0.00045	3.94E-05	0.281115	8.07E-06	2674	0.28109	−59.064	0.95049	0.28702	2931.93
	SM27-15	0.00054	9.95E-06	0.281065	1.16E-05	2684	0.28104	−60.8332	−0.77077	0.41254	3006.02

(Eu/Eu*= 1.32) anomaly has been recorded in one spot (spot 5; Fig. 10a). Average temperature calculated for tonalities using the equation of Watson et al. (2006) is T_{zircon} = 865 ± 11.9 °C (Table 1).

The isotopic composition of zircon crystals from the tonalite has low ratios of $^{176}Lu/^{177}Hf$ and present-day $^{176}Hf/^{177}Hf$. The former ranges from 0.00067 to 0.00139 (sample SM02), and from 0.00086 to 0.00173 (sample SM25), with an average of 0.0012 ± 0.000031. The latter ratio ranges from 0.28109 to 0.28114 (sample SM02), and from 0.28113 to 0.28117 (sample SM25), with an average of 0.28113 ± 0.0000072 (Table 2). Similar to tonalite (TTs), the trondhjemite (TRANG) has low $^{176}Lu/^{177}Hf$ and present-day $^{176}Hf/^{177}Hf$ ratios that range from 0.00031 to 0.00119 (Av. = 0.00056 ± 0.000086) and from 0.28108 to 0.28112 (Av. = 0.28109 ± 0.00001), respectively. The tonalite (TTs) and trondhjemite (TRANG) display initial $\varepsilon_{Hf}(t)$ values that are close to that of the Chondritic Uniform Reservoir (CHUR), with little variations (Fig. 10c). The tonalite (TTs) has positive $\varepsilon_{Hf}(t)$ values that range from 0.54 to 1.26 (sample SM02) and from 0.38 to 1.55 (sample SM25) with an average 0.67 ± 0.25609. However, zircon rims from samples SM02 (spots 10 and 12) and SM25 (spots 8 and 12) have negative $\varepsilon_{Hf}(t)$ values of (−0.58 and −0.26) and (−0.11 and −0.28), respectively. Compared to the tonalite (TTs), zircons from the trondhjemite (TRANG) have relatively low $\varepsilon_{Hf}(t)$ values that vary between −0.47 and 0.92, with an average close to zero (ε_{Hf} = −0.1 ± 0.39). Isotopic dates for zircon core and rim from sample SM2 yielded ages of 2700–2714 Ma and 2699 Ma, respectively (Fig. 9b). Similarly, core and rim ages from sample SM25 yielded 2700–2712 Ma, and 2655 (spot 8) and 2665 Ma (spot 12), respectively (Fig. 9c). The estimated ages for zircons from the trondhjemite (TRANG) show no distinct difference between core and rim, and yielded an age of 2660–2683 Ma. Furthermore, depleted mantle Hf model ages (T_{DM}) for the tonalite (TTs) and trondhjemite (TRANG) have been calculated and range from 2941 to 3007 Ma.

4.2.2. Potassic granites

Zircons from the potassic granite form sub- to euhedral elongated to elliptical crystals characterized by oscillatory zoning with darker rims overgrowing brighter metamict cores (Fig. 9f). A linear-zoned core is shown in a few crystals (Fig. 9f).

Compared to the tonalite, the zircons from the potassic granite have relatively high Th (135–2024.9 ppm) and U contents (404.4–5185.2 ppm). However, they share a common moderate Th/U ratio (0.2–0.5 ppm) of magmatic zircons with the tonalite. An inner bright core with resorbed edges, spot 5 in sample SM02, has lower Th- and U-contents similar to the element ranges of zircons from the tonalite. In the granite, the ranges, however, increase towards the dark rims (Fig. 9f, Table 1). On the normalized-chondrite REE diagram (Fig. 10b), the HREE and LREE of the zircons display a variable pattern. Comparable to the tonalite, in three spots (1, 4 and 6; SM01), the zircons have an enriched HREE pattern (La_N/Yb_N = 0.08–0.48). However, in spots 2 and 3 of sample SM01, the LREEs are more enriched (La_N/Yb_N = 4.01 and 1.81) and fractionated (La_N/Sm_N = 1.11–1.8). The patterns display negative and no Eu anomalies (Eu/Eu*= 0.69–1.14) (Fig. 10b). Average temperature calculated for potassic granite using the equation of Watson et al. (2006) is T_{zircon} = 921 ± 12 °C (Table 1).

The Lu-Hf isotopic composition of the potassic granite is characterized by slightly lower ratios of $^{176}Lu/^{177}Hf$ and present-day $^{176}Hf/^{177}Hf$ relative to those of the tonalites (Table 2). The

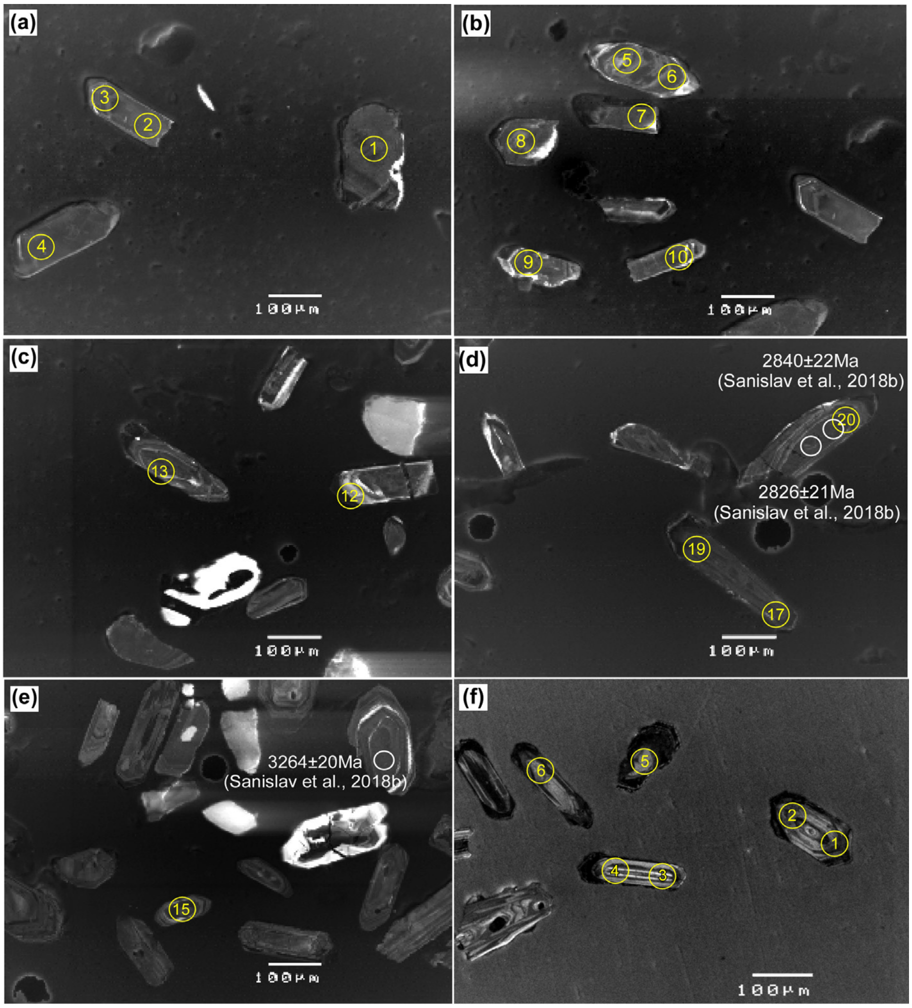

Fig. 9. Representative cathodoluminescence images of zircon crystals from tonalite (a–d), TRANG (e) and potassic granite (f). The yellow circles with numbers represent the spot analyses for chemical and isotopic compositions. The white circles represent the spots for ^{207}Pb/^{206}Pb zircon ages recorded by Sanislav et al. (2018b).

^{176}Lu/^{177}Hf ratios range from 0.00043 to 0.00167, and from 0.00018 to 0.00096, with an average 0.00065 ± 0.000019, whereas the ^{167}Hf/^{177}Hf ratios range between 0.28110–0.28116 and 0.28107–0.28112, with an average 0.2811 ± 0.000011, for samples SM23 and SM27, respectively.

The $\varepsilon_{\mathrm{Hf}}(t)$ values are near CHUR $\varepsilon_{\mathrm{Hf}}$ value similar to those from the TTs (Fig. 10c). However, the values fluctuate between positive (0.004–0.39) with a negative outlier ($\varepsilon_{\mathrm{Hf}} = -0.16$) in sample SM23, and negative (−0.77 to −0.03) with a positive outlier ($\varepsilon_{\mathrm{Hf}} = 0.95$) in sample SM27.

The zircon from the granite yielded isotopic ages of (2646–2685 Ma) that are comparable to those obtained from trondhjemite (TRANG).

5. Discussion

5.1. Petrogenesis of Neoarchean Geita granitoid

Generation of the TTGs melt results from either of two main mechanisms: partial melting of pre-existing basaltic rocks (Halla et al., 2009; Smithies et al., 2009; Almeida et al., 2011; Martin et al., 2014; Saki et al., 2021; Wu et al., 2023), or fractional crystallization of parental basaltic magma (Kamber et al., 2002; Kleinhanns, et al., 2003; Martin and Sigmarsson, 2005; Jagoutz et al., 2013; Liou and Guo, 2019; Smithies et al., 2019). For determination of either of the two mechanisms, trace elements play a crucial role. Despite the general controversy regarding the Archean TTGs, there is a consensus that they were derived from a hydrous basaltic source (Smithies, 2000; Martin and Moyen, 2002; Smithies et al., 2003; Maboko et al., 2006; Huang et al., 2013; Martin et al., 2014; Manya, 2016; Sanislav et al., 2014; Wu et al., 2023). Such consensus comes from the fact that the TTGs share common geochemical similarities with the modern high-silica adakites (HSA) that originated from basaltic slab-melting at a convergent plate boundary (Foley et al., 2002; Martin and Sigmarsson, 2005; Martin et al., 2005; Moyen and Martin, 2012; Laurent et al., 2014; Ganade et al., 2017; Liu et al., 2020). Additionally, experimental studies on natural and synthetic basalts proved that hydrous basalts are the pristine parental melt source of the TTGs (Martin and Moyen, 2002; Rapp et al., 2003; Martin et al., 2014).

The parental melt of the Archean potassic granite, on the other hand, is controversial. The source of the parental melt has been strongly debated. On the one hand, a mafic source has been advocated by some authors (Moyen, 2011; Laurent et al., 2014). On the other hand, a more felsic source, especially the pre-existing TTG, has been interpreted by others (Huang et al., 2013; Laurent et al., 2014; Sanislav et al., 2014). Moreover, melting of the metasediments (Jaguin et al., 2012; Laurent et al., 2014; Sanislav et al., 2014) might had a significant contribution in the formation of the melt source for the potassic granite.

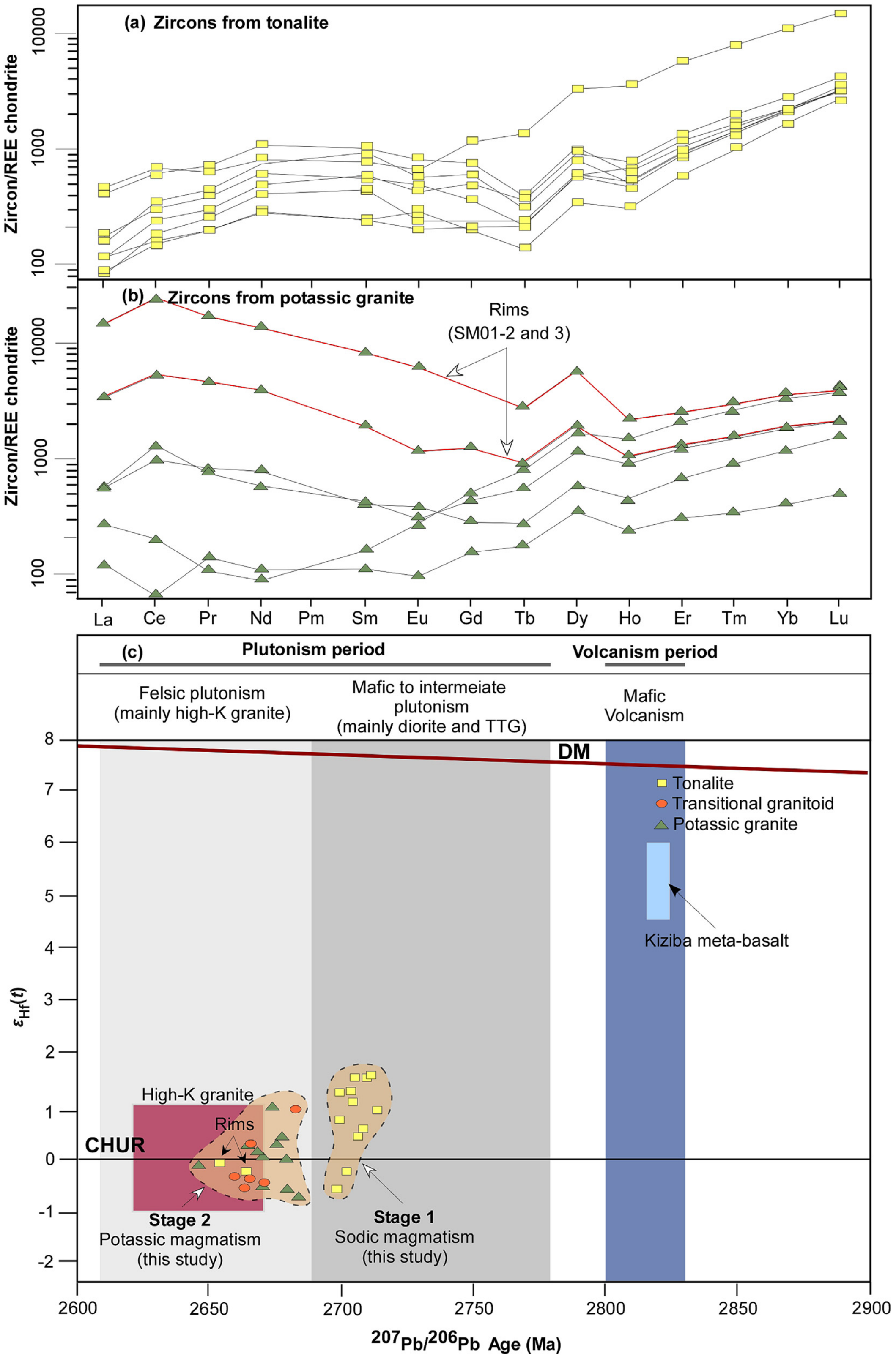

Fig. 10. Chondrite normalized REE diagrams for zircons form tonalite (a) and potassic granite (b). Chondrite values from Anders and Grevesse (1989). (c) Zircon $\varepsilon_{Hf}(t)$ vs. $^{207}Pb/^{206}Pb$ ages (Sanislav et al., 2018b) for tonalite, TRANG and potassic granite. Stages 1 and 2 of Geita granitoids correspond to the mafic to intermediate and felsic plutonism of the northern Tanzania Craton, respectively. Fields of magmatic zircon ages from various rock units of northern Tanzania Craton are after Sanislav et al. (2014, 2018a). Depleted mantle (DM) is after Blichert-Toft and Puchtel (2010).

5.1.1. Source and formation mechanism

Zircon chemistry (high Th/U ratio) and cathodoluminescence data (oscillatory zoning) together with the ^{207}Pb/^{206}Pb ages obtained by Sanislav et al. (2018b) indicate the crystallization ages for the majority of rocks. Moreover, the outermost bright discontinuous rims with low Th/U ratio of some zircons obtained from tonalite yield metamorphic ages of 2655, 2665 and 2700 Ma (Sanislav et al., 2018b; Table 2).

On the source rock discrimination diagram (after Bao et al., 2022; Sun et al., 2025), the tonalite and low-silica trondhjemite plot in the low K-mafic rocks whereas some of high-silica trondhjemite and potassic granite plot in the tonalites field (Fig. 11a). The latter results explain the overlap of some elements in various rock types on the Harker diagram (Fig. 3b–f). The TRANG straddles the line boundary between the high- and low-K mafic rock fields (Fig. 11a). The poor peraluminous character (ASI < 1.1) of the TTs, TRANG and potassic granite rules out the metasediments as a possible source rock (e.g., Sisson et al., 2005; Jaguin et al., 2012; Laurent et al., 2014; and references therein).

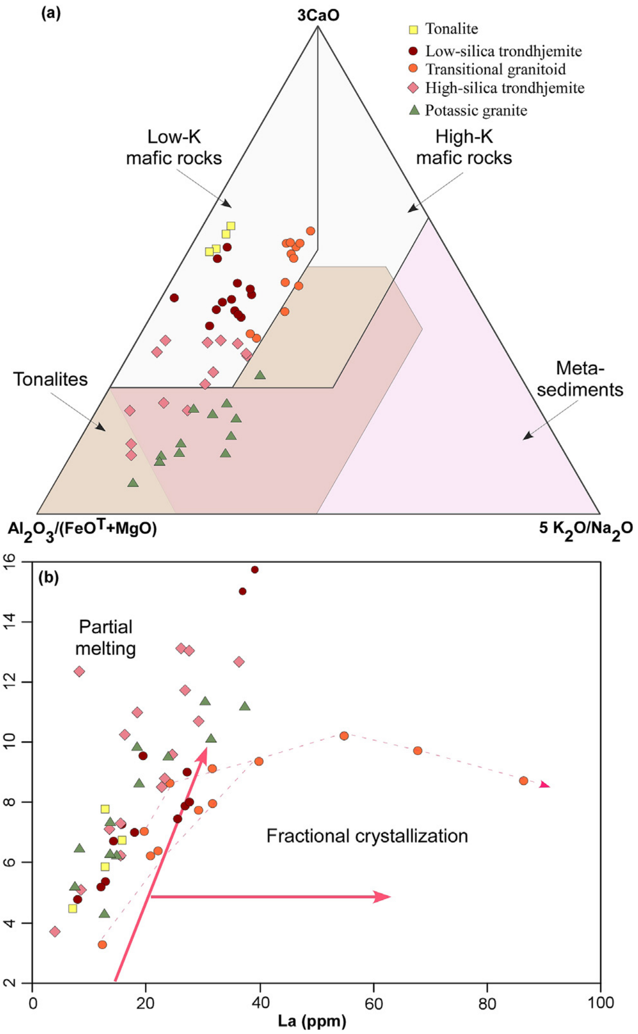

Fig. 11. (a) Ternary source diagram (after Bao et al., 2022; Sun et al., 2025) for discriminating sources of Neoarchean granitoids. The tonalite and low-silica trondhjemites, plot mainly within the low-K mafic rocks field. The high-silica trondhjemite and potassic granite plot mainly within the tonalites field. The TRANG plots close to the boundary between the low- and high-K mafic rocks fields. (b) La/Sm vs. La binary diagram (after Jiang et al., 2005) showing the partial melting and fractional crystallization trends (pink arrows). The TTs and potassic granite follow the partial melting path. The TRANG follows a fractional crystallization trend.

5.1.1.1. Tonalite and low-silica trondhjemite. HREE depletion, Sr enrichment, and the positive correlation between La/Sm ratio and La of the tonalite and low-silica trondhjemite are suggestive of partial melting rather than fractional crystallization (e.g., Martin and Sigmarsson, 2005, 2010; Halla et al., 2009; Martin et al., 2014; Wu et al., 2023). The latter conclusion is supported with the results of batch melting models on REE, multi-trace element and La$_N$/Yb$_N$ and Sr/Y vs. Yb$_N$ and Y, respectively, diagrams (Figs. 5a, b, 7a, b and 12b). However, HREEs depletion is argued by Kamber et al. (2002) to be an indicator for the melting of a basaltic precursor. The study rather suggests that the negative correlation between La/Yb ratio and FeO^T could point to fractional crystallization of amphibole and/or clinopyroxene (Kamber et al., 2002). Mesoscopic evidence in favor of the partial melting mechanism includes lack of co-magmatic mafic enclaves within the tonalite and low-silica trondhjemite, and of cumulate texture. Microscopically, zircon with oscillatory-zoned rims implies crystallization from a melt introduced by partial melting at a high-P metamorphic condition (e.g., Wu et al., 2009; Fig. 9e).

High Al$_2$O$_3$ content and slightly low K$_2$O/Na$_2$O ratio suggest that hydrous basalt could have been the source of the tonalite and low-silica trondhjemite (e.g., Smithies, 2000; Maboko et al., 2006; Moyen and Martin, 2012; Huang et al., 2013; Manya, 2016; Moyen and Laurent, 2018). At great depths and water-saturated conditions, low-T and high-P basalts would generate sodic, mainly trondhjemitic, melts, e.g., the early-formed (2699–2714 Ma) tonalitic to trondhjemitic melts (e.g. Prouteau et al., 2001; Weinberg and Hasalová, 2015) (see section 5.3). The latter conditions favored the formation of garnet-rich restite and hence explain the HREE depletion in the co-existing tonalitic to trondhjemitic melt. The present study suggests that Kiziba metabasalt, which originated from a primitive mantle source that is more enriched than modern depleted mantle (Cook et al., 2016), has been likely the precursor of the Geita tonalitic and trondhjemitic melts. Additionally, from a geochronological perspective, the overlapping dates between the age of zircons' inherited cores (2826–2840 Ma; Sanislav et al., 2018b) from tonalite and the eruption age of Kiziba basalt (~2823 Ma, Manya and Maboko, 2008; ~2830 and ~2820 Ma, Cook et al., 2016) imply that the tonalite and low-silica trondhjemite most probably originated from the partial melting of the mafic component of Kiziba Formation. Archean TTGs originated from the partial melting of a primitive mantle-derived basalt have been documented from the Pilbara Craton, NW Australia (Smithies et al., 2009).

5.1.1.2. High-silica trondhjemite. The progressive decrease in MgO, Al$_2$O$_3$, FeO^T, TiO$_2$, P$_2$O$_5$, Na$_2$O, and increase in K$_2$O and K$_2$O + Na$_2$O (Fig. 3a–l) from tonalite to the high-silica trondhjemite imply that the high-silica trondhjemite could have been a fractionate of tonalite (e.g. Ustunisik and Kilinc, 2011). Apart from the marked enrichment of mobile elements K and Ba, and strong HREE depletion of the high-silica trondhjemite, the high-silica trondhjemite and tonalite have a very similar normalized multi-element profile (Fig. 6a and c). At low degree of fractionation, K and Ba have high affinity to stay in the silicate melt rather than partitioning into the crystalline solid, particularly in the absence of fractionating K-feldspar (Martin and Sigmarsson, 2010). At this stage, concentrations of the incompatible elements in the residual melt and in the initial tonalitic magma would be very close. Fractional crystallization is further evidenced by high silica content and strong depletion in the less incompatible HREEs and Y, and their corresponding high La$_N$/Yb$_N$ (13.4–114.8) and Sr/Y (up to 333) ratios (e.g., Bédard, 2006; Halla et al., 2009; Martin and sigmarsson, 2010; Smithies et al., 2019). However, on La/Sm vs. La diagram (Fig. 11b), the high-silica trondhjemite and tonalite share a common partial melting trend that could be attributed to

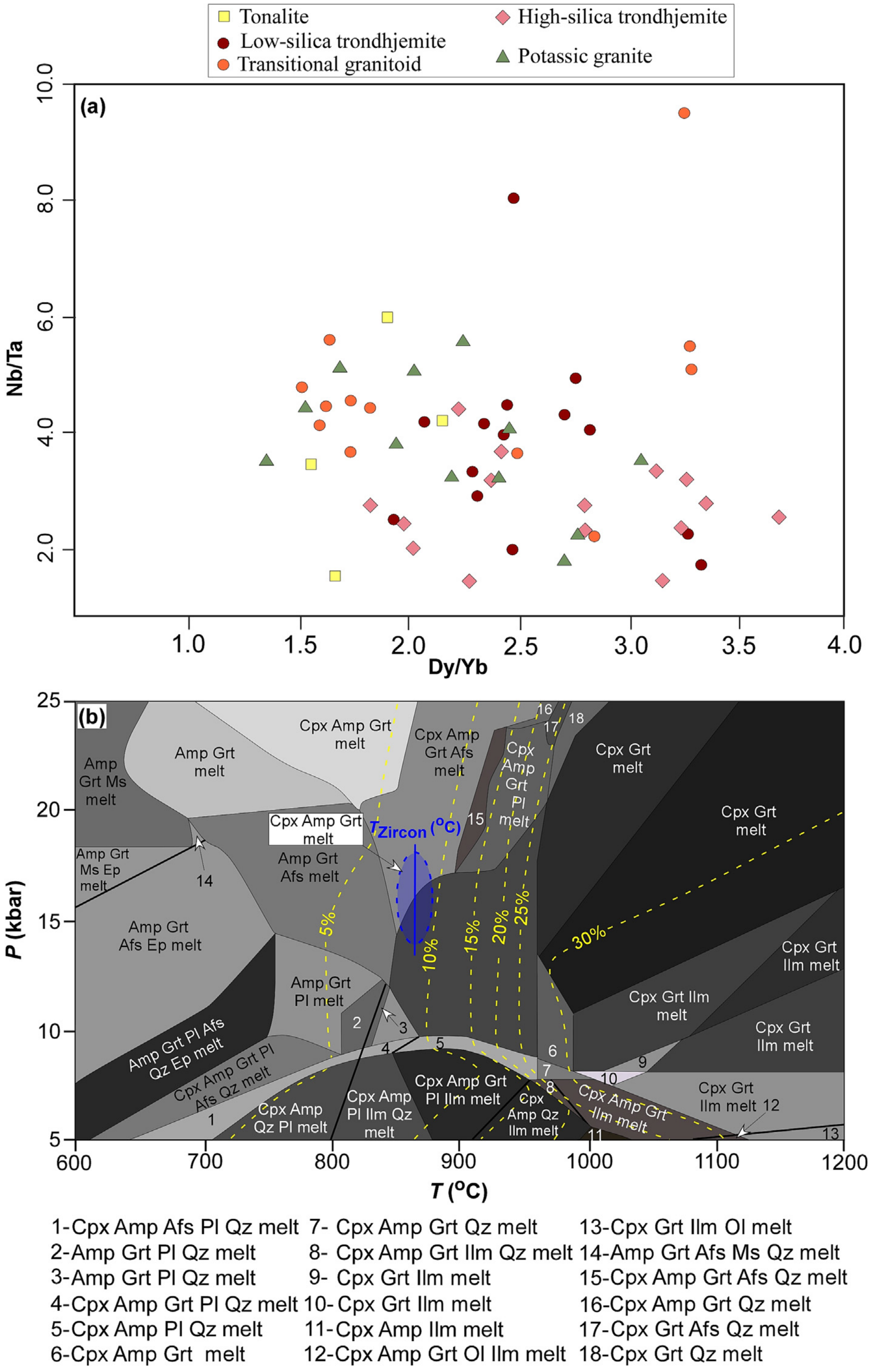

Fig. 12. (a) Nb/Ta vs. Dy/Yb diagram, after Liu et al. (2023), shows no correlation between Nb/Ta and Dy/Yb ratios of the Neoarchean Geita granitoids. (b) *P-T* psuedosection estimated for Kiziba basalt (data from Manya and Maboko, 2008) using Perple_X 6.7.9 software. *P-T* range for thermodynamic modeling calculated based on zircon thermometry and mineral phases from batch melting models. Dashed yellow lines represent contours for the generated melt (wt.%). Blue circle shows the *P-T* range calculated for the Kiziba basalt. T_{zircon} (°C) is the average temperature calculated for the tonalite by classic Ti-in-zirccon thermometry. Afs: Alkali feldspar; Aln: Allanite; Amp: Amphibole; Bt: biotite; Cpx: Clinopyroxene; Ep: Epidote; Grt: Garnet; Ilm: Ilmenite; Ol: Olivine; Pl: Plagioclase; Qz: Quartz (Whitney and Evan, 2010).

the original La/Sm ratio of the parental tonalitic magma. Bédard (2006) and Moyen et al. (2007) suggested that fractional crystallization of a parental tonalitic melt generated by partial melting of a basaltic protolith plays a significant role in modification of the TTG composition, particularly the high Sr/Y ratio. On the Sr/Y vs. Y diagram, the trondhjemite plots are consistent with the hornblende fractionation path of Bédard (2006) (Fig. 7b). High Sr/Y ratios together with high SiO_2 content (>70 wt.%; Supplementary Data 1, Table S1) are suggestive of a hornblende fractionation (e.g. trondhjemite from the Minto Block, Northeastern Superior Province (Bédard, 2006). Moreover, high ratios of Sr/Y and positive Eu/Eu* anomaly indicate accumulation of plagioclase in the high-silica trondhjemite (Fig. 8c). However, marked low LREE (Fig. 5c) of the latter could be attributed to crystallization of early-formed epidote and/or allanite (e.g., Dessimoz et al., 2012). The fractional crystallization could explain the vast distribution of high-silica trondhjemite on the Na_2O-K_2O-CaO ternary diagram of Moyen et al. (2003). At the mesoscopic scale, chilled trondhjemite near the contact against Kiziba basalt upholds the magmatic origin of the former.

5.1.1.3. Transitional granitoid (TRANG). The TRANG (2660–2683 Ma) contains, in places, fine grained more mafic xenolith. In contrast to the older TTs, the younger TRANG is less depleted in HREE and HFSE, and typically displays a fractional crystallization trend (Figs. 4a, 5b, 6b and 12b). The fractionation process is further manifested by the Eu anomaly that is negatively and positively correlated with K_2O and (Na_2O + CaO), respectively (e.g., Kleinhanns et al., 2003; Fig. 4a and b). Moreover, the TRANG is more enriched in LREE and LILE, and has a slightly high K_2O/Na_2O ratio and high (FeO^T + MgO + MnO + TiO_2) content, which implies a high-K mafic source relative to the TTs (Figs. 3l, 5b, 6b and 11a). Chronologically, inherited zircon cores yielded an age of 3264 ± 20 Ma (Sanislav et al., 2018b) that correlates well with zircon ages recorded from the Dodoman Supergroup (3000–3600 Ma, Kabete et al., 2012) that is assumed to represent the older part of the Tanzania Craton. Zoned crystals with inherited cores mantled by rims exhibiting well-developed growth zoning (Fig. 9e) are further evidence of the magmatic origin of the TRANG magma. The core (inherited) and mantle zircon zoning in some crystals imply that the trondhjemitic magma could have been Zr-oversaturated (e.g. Corfu et al., 2003). The dual mantle (wide range of SiO_2 and high K, Ba, Sr, Cr and V and ferromagnesian oxides; MgO + FeO^T + MnO + TiO_2) and crustal isotope signature (low $\varepsilon_{Hf}(t)$ value) might imply a metasomatized mantle-melt (e.g., Halla et al., 2009; Laurent et al., 2014) that could have been the source of the TRANG. The latter conclusion is confirmed by a group of lamprophyre dykes cutting across the Nyanzian unit (Sanislav et al., 2015).

5.1.1.4. Potassic granite. Similar to the tonalite and low-silica trondhjemite, partial melting was the most probable mechanism responsible for the generation of potassic granite. The potassic granite has a relatively low La_N/Yb_N ratio (7.2–56.4) that is inconsistent with its high SiO_2 content (e.g., Halla et al., 2009; Smithies et al., 2009), which is the highest among the Geita granitoids. The latter inconsistency implies generation of the granite by partial melting of a low La_N/Yb_N source rather than by fractional crystallization. Moreover, partial melting is further supported by less depletion in the HREE of the granite relative to the high-silica trondhjemite, which implies lower modal abundance of HREE-host minerals (e.g., amphibole; Kamber et al., 2002) in the residue (Fig. 5c and d), and by the positive correlation between La/Sm and La (Fig. 11b). The potassic granite shows a compositional trend similar to that of the TTs (Fig. 3a–l) with relatively high SiO_2 and alkali (Na_2O and K_2O) contents, and strong enrichments of the LILEs (Rb, K and Pb) suggesting derivation of the granite from a more differentiated melt rather than a mafic parentage. Moreover, the pronounced enriched LREE pattern (Fig. 10b) and high U and Th contents, particularly of some zircon rims (Fig. 9f), imply a transition into a more evolved melt (Fig. 10b). High SiO_2 and low MgO, Sr and Ba contents together with low $\varepsilon_{Hf}(t)$ value (Fig. 10c) indicate generation of the potassic granite from reworking of a crust material (Joshi et al., 2016; Halla et al., 2017). The metamorphic ages of zircon rims from tonalite are comparable to crystallization ages of zircon from the potassic granite. The above-mentioned criteria suggest not only that the granite and the tonalite are genetically related, but also imply that the potassic granite was, most probably, generated as a mobilizate that accompanied the metamorphism of tonalite.

5.1.2. The improbability of mantle-melt interaction

The common zircon isotopic composition implies that Neoarchean Geita granitoids share a common evolution path that began with TTs to the TRANG and ended up with the potassic granite. Moreover, low values of, and inhomogeneity in $^{176}Lu/^{177}Hf$ and $^{176}Hf/^{177}Hf$ isotropic ratios of zircons are suggestive of derivation from a crustal reservoir (e.g., Belousova et al., 2006) with insignificant mantle wedge contribution (e.g., Martin and Moyen, 2002; Mshiu and Maboko, 2012). Furthermore, low zircon $\varepsilon_{Hf}(t)$ values (ε_{Hf} = +2 to −1) relative to that of the contemporaneous depleted mantle (Fig. 10c) infer the involvement of crustal component in the generation of the granitoids (e.g., Laurent et al., 2014). Additionally, high SiO_2, Al_2O_3, contents, high Rb, Th and U concentrations, and low Mg# and transition elements (Cr and Ni) values suggest a significant participation of crustal materials in the generation of Geita granitoids (e.g., Martin and Moyen, 2002; Mshiu and Maboko, 2012).

In a similar way, geochemical evidence in favor of significant crustal contribution in the generation of Archean TTG includes depletion in Ni (<40 ppm), Cr (<50 ppm) and Mg# (~ < 50) in Early Archean and some Neoarchean TTGs (Smithies, 2000). Moreover, experimental work shows that Mg# (~ >50) together with high Cr and V contents has been used as geochemical indicators for mantle peridotite-slab melt interaction (Rapp, 1997; Smithies, 2000). The Neoarchean Geita granitoids, except for two samples with Mg# of 53 and 48, have Mg# value that ranges from 7 to 45.

5.2. Residual minerals and implication for metamorphism

During partial melting, the mineralogy of the restite overwhelmingly governs the chemical composition of the melt (García-Arias et al., 2012). Moreover, the mineralogy of the residual assemblage would reflect the metamorphic conditions at which the melt was produced (Wu et al., 2023; and references therein). The behavior of trace elements is greatly influenced by the coexisting residual mineral phases, and/or the partitioning coefficient ratios of some elements. For example, HREEs and Y have a great affinity to be incorporated into garnet (Martin, 1987; Martin et al., 2005; Moyen and Stevens, 2006; Halla et al., 2009). Accordingly, existence of residual garnet would suppress HREEs and Y contents in the melt. Nb and Ta partition into rutile and amphibole (Foley et al., 2002; Maboko et al., 2006), whereas Ca, Na, Sr (Sr < 400 ppm) as well as P partition into plagioclase (Martin and Moyen, 2002; Halla et al., 2009; García-Arias et al., 2012; Tsay et al., 2014).

5.2.1. Feldspar

Positive Sr (Sr/Sr*=1.16–11.68), and negative Y anomalies with corresponding high Sr/Y (45.6–213.4; Sr > 400 ppm) ratio and high CaO + Na_2O (5.29–9.81) contents are attributed to the lack of plagioclase in the restite of the tonalite and low-silica trondhjemite (e.g., Martin, 1999; Martin and Moyen, 2002; Martin et al., 2005; Huang et al., 2013). Potassic granite, on the contrary, shows slightly negative to slightly positive Sr anomalies (Sr/Sr* = 0.995–2.12), and has lower Sr/Y ratio (21–174.2; Sr = 168.5–479.9 ppm) and Na_2 + CaO contents (4.76–6.27) that confirm the presence of plagioclase in the residue. Similarly, strong negative P anomaly in the granite could be attributed to incorporation of P in the residual feldspar during partial melting of the TTs (e.g., García-Arias et al., 2012; and references therein). High water content and metamorphic pressure lower the plagioclase stability field as a residual phase (Palin et al., 2016; Marimon et al., 2022). The latter statement implies that crystallization of the tonalite and low-silica trondhjemite took place beyond plagioclase stability field at a water-saturated condition and great depth, and that crystallization of potassic granite parental melt might have been at shallower depth under fluid-undersaturated condition (e.g. Martin and Moyen, 2002; Maboko et al., 2006; Tsay et al., 2014; and references therein). Based on zircon chemistry, positive Ce and negative Eu anomalies of the tonalite (Fig. 10a) suggest crystallization at oxidizing condition (e.g., Peck et al., 2001; Moyen and Martin, 2012). Eu in the oxidation state (Eu^{3+}) is more incompatible and could not fit the plagioclase structure. Accordingly, the negative Eu anomaly in the tonalite might be attributed to the crystallization of an original rather than residual plagioclase phases (Fig. 5a, b and d). The latter conclusion is consistent with the negative Eu anomaly of the parent Kiziba basalt (Cook et al., 2016). Moreover, variability of Eu anomaly of the potassic granite from strong negative to slightly positive anomaly could be attributed to the diversity of TTs source components, i.e. tonalite, low-silica trondhjemite and high-silica trondhjemite.

5.2.2. Amphibole

Negative Ti anomaly in the tonalite, low-silica trondhjemite and potassic granite (Fig. 6a, b and d) most probably demonstrates the presence of Ti-host residual phases (rutile, ilmenite and amphibole). Rutile has a Nb/Ta partition coefficient ratio (D_{Nb}/D_{Ta}) of less than 1, and hence has the ability to decouple Ta from Nb (Foley et al., 2000, 2002). The experimental partition data reveal that rutile imparts a high Nb/Ta ratio to the melt (Foley et al., 2002). The latter result is inconsistent with the low Nb/Ta ratio in the Geita granitoids. Amphibole, on the other hand, can decouple Ta and Zr from Nb and Hf (Foley et al., 2002). In their octahedron M1 sites, amphiboles can accommodate the ionic radii of either Ta or Nb. The partitioning coefficient ratio (D_{Nb}/D_{Ta}) depends on the bulk Mg# of the coexisting melt (Foley, 2008). Amphiboles with low < 70 Mg# (bulk Mg# Av. of the coexisting melt ~40–45) have a D_{Nb}/D_{Ta} higher than 1, and fractionates Nb from Ta. Low Ti content of the amphibole implies Nb/Ta fractionation (Foley, 2008), and together with the negative Ti anomaly of the coexisting melt (now the tonalite, low-silica main trondhjemite mass and potassic granite) could be attributed to the presence of ilmenite in the restite (Fig. 6a, b and d). Similarly, amphibole can decouple Nb from La, Sm from Zr, and Rb from K (Foley et al., 2002; Maboko et al., 2006; Foley, 2008). Accordingly, in the older basalt-derived TT and potassic granite, low K/Rb, Nb/Ta and Nb/La ratios, and high Zr/Sm ratios are suggestive of Mg# bearing-residual amphibole that has been responsible for the fractionation of Nb and Ta. Additionally, Sm partitions more readily into clinopyroxene relative to Zr (Rapp et al., 2003), and hence high Zr/Sm ratio of the coexisting melt could imply the presence of residual clinopyroxene.

5.2.3. Garnet

Residual garnets are responsible for high La_N/Yb_N and Sr/Y ratios in the coexisting melt (e.g., Sanislav et al., 2014; Tsay et al., 2014; Kwelwa et al., 2018a). These ratios are consistent with trace elements composition of the Geita tonalite and low-silica trondhjemite (e.g., Martin et al., 2005; Maboko et al., 2006; Castillo, 2012; Sanislav et al., 2014; Tsay et al., 2014; Kwelwa et al., 2018a). Based on trace element geochemistry, Moyen (2011) classified the Archean sodic TTG into three models: model one, two and three; that comprise rocks formed at low-, medium-, and high-pressure conditions. La/Yb and Sr/Y ratios show that residual garnet was stable at medium pressure (ca. 15 kbar) metamorphic condition (model 2 of Moyen, 2011). However, slight deviation from the model can be explained by the difference in percentage of the residual minerals. Potassic granite, on the other hand, has a relatively low La/Yb and Sr/Y ratios and flatter HREE patterns. Therefore, garnet has not been a distinct residual phase during the crystallization of the coexisting melt (e.g. Halla et al., 2009).

In sum, it is suggested that the Archean Geita tonalite and low silica trondhjemite evolved through partial melting of garnet-amphibolite rather than rutile-bearing eclogite (e.g., Foley et al., 2000, 2002; Wu et al., 2023). Potassic granite, on the other hand, was generated at a lower (garnet-free) amphibolite facies metamorphic condition. Moreover, Sr/Zr vs. Dy/Yb plots (Fig. 13a) show that TTs follow the trend of increasing amphibole and reducing plagioclase during fluid-fluxed partial melting, whereas potassic granite is consistent with the residue-lacking water trend (e.g., Marimon et al., 2022).

The latter conclusion is consistent with trace element modeling (Figs. 5a–d, 6a–d and 7a, b). In that model, the fractionated/residual minerals either from the parental magma or source melt are estimated using Rayleigh's law ($C_L/C_0 = 1 - F^{(D-1)}$) and Batch melting equation ($C_L/C_0 = D_{Rs} + F(1 - D_{Rs})$), where: C_L is the melt composition; C_0 is the source composition; D_{Rs} is the total partition coefficient of residual minerals; and F is the melt fraction. The partition coefficients of the element (K_d) are obtained from the literatures (Rollinson, 1993; Bédard, 2006; Rollinson and Pease, 2021; and the database http://earthref.org/GERM; Supplementary Data 2). The source compositions (C_0) in each model are represented by average trace elements of either Kiziba basalt or the TTs in batch melting models (Figs. 4a, b, d and 5a, b, d), or of the more mafic tonalite in the fractional crystallization model (Figs. 4c and 5c). In the batch melting models, the low-silica trondhjemite (TTs) is strongly enriched in LREE and heavily depleted in HREE, has high Sr content relative to the other TTs, and is considered to be the residue accompanied the potassic granite (Fig. 5c, d). However, the residue of the Kiziba amphibolite could have been delaminated (see section 5.5). In the fractionation model, early-formed minerals of the tonalitic melt are considered the fractionating phases (e.g., Bédard, 2006). The Mombaça TTG gneisses, Tróia Massif, N Borborema Province, NE Brazil, with a similar trace element geochemistry have been interpreted to be generated as medium pressure TTGs at the garnet zone of the upper amphibolite facies (Ganade et al., 2017).

5.3. Thermodynamic modeling

A thermodynamic model was performed to refine *PT* conditions for the anatexis of the source rocks responsible for the generation of tonalite and low-silica trondhjemite (TTs), using the Perple_X 6.7.9 software (http://www.perplex.ethz.ch). The calculation is performed using Na_2O-CaO-K_2O-FeO-MgO-Al_2O_3-SiO_2-H_2O-TiO_2 (NCKFMASHT) system, with calculated iron as FeO^T, and negligible P_2O_5 content (e.g., Saki et al., 2021; Sun et al., 2021). Thermodynamic database (the file hp02ver.dat) of Holland and Powell (2011), together with a solid solution model was used. The solution model is melt (G) for melt, Augite (G) for clinopyroxene and cAmph (G) for amphibole from Green et al. (2016), Gt (W) for garnet and Ilm (WPH) for ilmenite from White et al. (2014). Pseudosection is drawn upon $T = 600–1100$ °C and $P = 5–22$ kbar for the bulk chemical composition of the source rocks; Kiziba basalt (Manya and Maboko, 2008; Fig. 12b). The mineral and melt phases were calculated in wt.% to correlate the resultant phases with the trace element modeling and to contour the melt isopleths. The output data are presented in the Supplementary Data 3.

Following the workflow proposed by Saki et al. (2021), the integration of residual phases from batch melting models and temperature estimated from classic Ti-in-zircon thermometry with the result obtained from thermodynamic modeling shed the light on the *PT* conditions of partial melting of the Kiziba basalt. Presence of residual mineral association (Cpx + Gart + Amp) and the degree

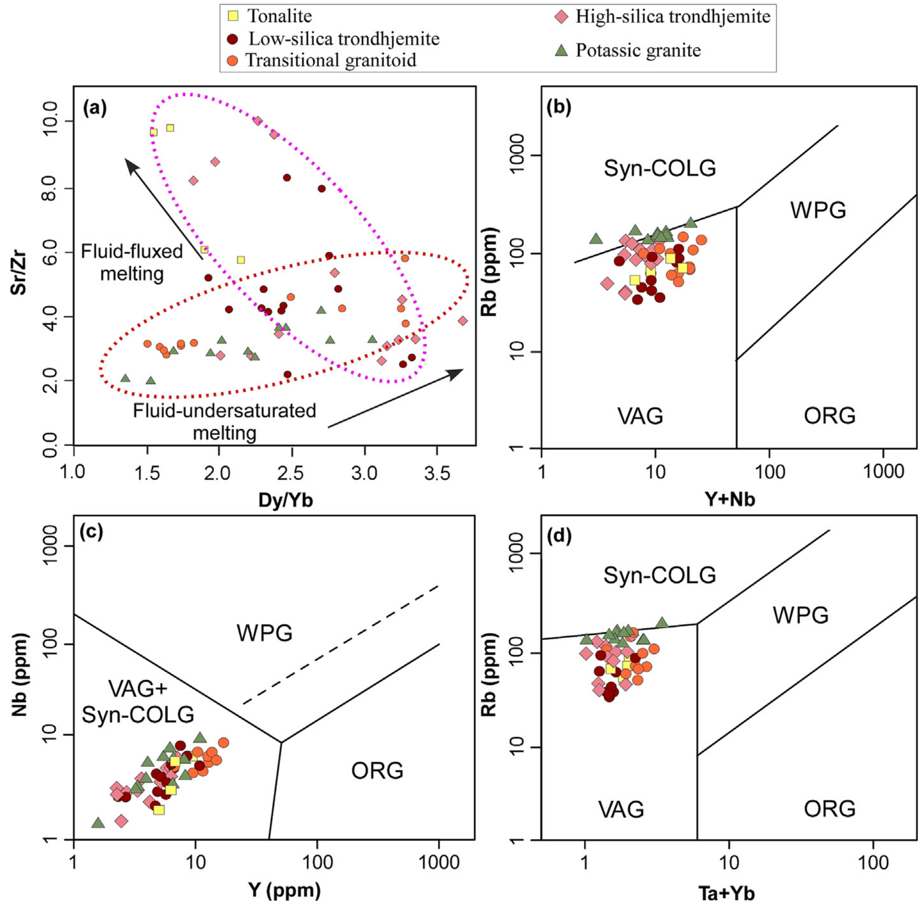

Fig. 13. (a) Two partial melting trends of Archean basalt, based on Sr/Zr vs. Dy/Yb diagram, after Marimon et al. (2022), at fluid saturated and undersaturated conditions. (b–d) Tectonic discrimination diagrams of Pearce et al. (1984). Neoarchean Geita granitoids occupy the fields of volcanic arc (VAG) granites.

of partial melting (5%–10%), consistent with the average estimated temperature (~865 °C) delineate the suitable condition for the partial melting event (Fig. 12b). The latter result implies that partial melting of the Kiziba basalt occurred at moderate *PT* condition (14–18 kbar and ~865 °C) of the upper amphibolite facies.

5.4. The tectonic setting

Archean geodynamic has long been a matter of enduring argument (Nair and Chacko, 2008; Van Hunen et al., 2008; Moyen and Martin, 2012; Martin et al., 2014; Marimon et al., 2022; Hastie et al., 2023). Orogenic (Martin et al., 2005, 2014; Manya, 2016; Marimon et al., 2022; Wu et al., 2023) and anorogenic (Whalen et al., 2002; Bédard, 2006; Smithies et al., 2009; Keller and Schoene, 2012) tectonic models have been proposed. Tectonic setting of the Geita Archean granitoids is determined using primarily geochemical data. Invalidity of the anorogenic (intraplate) setting for the Geita granitoids stems from the calc-alkaline to alkali-calcic geochemical signatures the rocks display (e.g., Laurent et al., 2014; and references therein). On tectonic setting discrimination diagrams, the Neoarchean Geita granitoids occupy the volcanic arc granite fields of Pearce et al. (1984) (Fig. 13b–e). The latter diagrams, although not properly applicable to the Archean rocks (Pearce et al., 1984), have been approved and used by some authors (Moyen and Laurent, 2018). Patterns of highly fractionated REEs (Fig. 5a–d) together with the distinctive negative Nb-Ta-Ti anomalies on the multi-elements spidergrams (Fig. 6a–d) imply that the Geita granitoid parental magmas were subduction-related. However, La_N/Yb_N ratios of the TTs (11–159), TRANG (7.8–72.5) and potassic granite (7.2–56.4) are inconsistent with the REEs signature of modern arc magma ($Y \geq 25$, $Yb \geq 2.5$ and $La_N/Yb_N < 10$; Martin, 1999) (e.g., Harris and Bédard, 2014; and references therein). Modern intermediate-felsic arc rocks have higher HREE concentrations than Archean granitoids. They exhibit positive Nb/Ta–Dy/Yb correlation (Fig. 12a) whereas the Archean rocks show no correlation (Liu et al., 2023; and references therein). The latter criteria are attributed to partial melting of a metasomatised mantle wedge above a dehydrated subducting slab (Liu et al., 2023). High La_N/Yb_N ratio of the Geita granitoids is attributed mostly to incorporation of the HREE into amphibole/garnet-rich restite (see sections 5.2.2 and 5.2.3). On the La_N/Yb_N vs. Yb_N diagram of Martin (1986) and Sr/Y vs. Y diagram of Drummond and Defant (1990), a few samples of the TRANG plot within the arc magmatic rock field (Fig. 7a and b), which together with the dual mantle-crust signature (see section 5.1.1.3) imply that the rocks might have been generated by contribution of a metasomatised mantle melt source rather than being a proper arc rocks (Fig. 7a and b). Although the Geita TTs and high-silica adakites share common geochemical characteristics, the adakites display a relatively high Mg# value and Cr content that are attributed to mantle-slab interaction (e.g., Smithies, 2000), a style that was not efficient in the generation of the Geita granitoids. Thus, the Neoarchean TTs and potassic granite could be interpreted to be generated in a geodynamic tectonic regime comparable to subduction-related setting, but with a style that differs from modern arc-settings (e.g., Moyen and Laurent, 2018).

Additionally, from the structural point of view, and based on a detailed fieldwork supported by aeromagnetic data, Sanislav et al. (2018b) recorded a crustal scale, ~800 m wide and 50 km long, shear zone that separates the TTG from the mafic metavolcanics of the Kiziba Formation (Fig. 1b). The shear zone is dominated by the TTGs (Sanislav et al., 2018b), and has been active from 2640 to 2690 Ma, a time period that overlaps well with the TTs magmatism. The fact that the shear zone and the TTs share common structure elements, intense steeply-dipping E–W-trending foliation and sub-horizontal stretching lineations (Fig. 3c and g presented in Sanislav et al., 2018b), together with their overlapping dates imply that a significant ductile deformation has been active during the TTs magmatism (e.g. Sanislav et al., 2018b). The linear style of the shear zone that is dominated by intense nearly-vertical foliation with dominant sub-horizontal stretching lineations is consistent with horizontal shortening mechanism that was responsible for terrane accretion, a tectonic regime that is comparable to the modern-day oblique convergence (e.g. Percival et al., 2006; Czarnota et al., 2010; Manikyamba and Kerrich, 2012). Crustal scale linear style shear zones indicative of terrain accretion have been documented worldwide. Examples include the Yilgarn Craton (Cassidy et al., 2006; Blewett et al., 2010), the Superior Province (Card, 1990; Polat et al., 1998) and the Dharwar Craton (Chadwick et al., 2001; Manikyamba and Kerrich, 2012).

5.5. Proposed tectonic models of worldwide Archean granitoids in comparison with Geita granitoids

Zircon ages from the Geita TTs coincide with the crustal growth peak evolution (2700–2650 Ma) of the Tanzania Craton suggested by Sanislav et al. (2014) (Fig. 10c). Worldwide, the Geita TTs belongs to the younger (post-3.0 Ga) phase of the Archean TTG (Smithies, 2000). The potassic granite and TRANG yield zircon ages of (2646–2685 Ma) and (2660–2683 Ma), respectively, that are comparable to the formation age of the northern Geita high-K granites (~2620–2680 Ma; Sanislav et al., 2014), and extend close to the end of the plutonic activity of the Tanzania Craton (~2620 Ma; Sanislav et al., 2014, 2018a; Fig. 10c).

An example of Archean TTGs generated at intraplate tectonic setting includes the primitive mantle-related basalt of the Pilbara Craton, NW Australia (Smithies et al., 2009). Subduction-related TTG model proposes that the original melt could have originated either at the base of a thick overriding oceanic crust/plateau (Huang et al., 2013; Manya, 2016; Wu et al., 2023) or from the subducted slab (Martin and Moyen, 2002; Smithies et al., 2003; Ganade et al., 2017). Simultaneous melting of the overriding and subducted plates has been recorded (Halla et al., 2009; Almeida et al., 2011). Examples of TTGs originated at oceanic plateau settings have been documented from Fiskenæsset, SW Greenland (Huang et al., 2013), and from Katoro TTG, Sukumaland (Wu et al., 2023) and Buzwagi mine TTG, Nzega (Manya, 2016) greenstone belts, North Tanzania. TTGs generated by slab melting have been recorded from the Tróia Massif, N. Borborema Province, NE Brazil (Ganade et al., 2017), and Eastern Liaoning Range region, northeastern North China Craton (Sun et al., 2024). TTGs generated from oceanic plateau-slab melt mixed sources have been recorded from Karelian and Kola Cratons, the Fennoscandian Shield (Halla et al., 2009), and the Rio Maria granite-greenstone terrain, SE Amazonian Craton (Almeida et al., 2011).

The Geita TTs share common characteristics with the TTGs of the oceanic-plateau model recorded from northern Tanzania (Greenstone belts: Katoro TTG (Wu et al., 2023) and Buzwagi mine TTG (Manya, 2016)), and Atlantic (Fiskenæsset complex, southwest Greenland: Huang et al., 2013) cratons. However, based on strong Nb, Ta and Ti anomalies, Fiskenæsset TTG was generated at eclogite facies condition (Huang et al., 2013). Additionally, average $\varepsilon_{\mathrm{Hf}}(t)$ (+1.90 ± 0.50 and +2.07 ± 0.33) measured from zircons of the Katoro TTG is higher than those from the Geita TTs. Experimentally, whether there has been a mantle contribution during slab melting model or not is controversial. It depends to a great extent on the attitude of the subducting slab, the depth at which the partial melting takes place, and the geothermal gradient.

For example, according to Martin and Moyen (2002), at great depths (behind plagioclase stability field) melting takes place at the base of a thick mantle wedge and consequently a great feasibility for mantle-melt interaction. Smithies et al. (2009), on the other hand, advocate for slab attitude and geothermal gradient as the main factors controlling mantle-melt interaction. Accordingly, the flat subduction with a high geothermal gradient favor slab melting rather than mantle wedge metasomatism via slab dehydration (Smithies et al., 2009). An example of the flat subduction model includes the medium-pressure TTGs of the Tróia Massif, N Borborema Province, NE Brazil (Ganade et al., 2017). Almeida et al. (2011) reported high-, medium-, and low-pressure TTGs from Rio Maria granite-greenstone, SE Amazonian Craton. A mixed model proposed by Almeida et al. (2011) for the three TTG groups concludes that slab melting of the high-and medium-pressure TTGs took place at different depths with significant mantle-melt interaction. Low-pressure TTG, on the other hand, was generated at the base of a thickened oceanic crust with no mantle contribution.

Medium-pressure Geita TTs, in terms of inferred pressure and insignificant mantle signature, are comparable to the TTGs of the N. Borborema Province, but inconsistent with the high- and medium-pressure TTGs of Rio Maria granite-greenstone, SE Amazonian Craton.

Apart from the slightly lower K_2O content (Figs. 1a and 4b), the Geita potassic granite shares similar chemical composition with the Neoarchean high-K granites of the Nzega and Musoma-Mara Greenstone Belts, N Tanzania (Mshiu and Maboko, 2012; Manya, 2016). The geochemical characteristics of the potassic granite are similar to those of the Neoarchean biotite granite (Fig. 4a) that is recorded from the Dharwar Craton, S. India (Mshiu and Maboko, 2012), and is interpreted to be derived from subduction-related partial melting of the TTG (e.g. Mshiu and Maboko, 2012; Laurent et al., 2014).

5.6. Possible tectonic models of the Neoarchean Geita granitoids

The origin of Kiziba basalt has been controversial. A back arc setting with an enriched mantle source that resulted from the interaction of MORB melt with a slab melt has been suggested (Manya and Maboko, 2008). Cook et al. (2016), on the other hand, argued that Kiziba basalt was originated from a primitive mantle source in an oceanic plateau-like setting. Archean oceanic plateaus (up to ca. 50 km thick; Bédard et al., 2013; and references therein) and crusts (minimum ~15 km thick, close to that of modern oceanic plateaus; Smithies, 2000) have been thicker, hotter and consequently more buoyant than their present-day counterparts (Martin et al., 2014; Liu et al., 2022). Buoyancy is compensated at the base of the plateau by eclogitization, a process that forces the plateau to subduct into the mantle (e.g. Martin et al., 2014). A delay in eclogitization of the oceanic crust promotes the flat subduction (e.g., Gutscher et al., 2000b; Liu et al, 2022).

The Geita granitoids share a common subduction-related tectonic setting with Archean TTGs mentioned in section 5.5. Based on the slight discrepancies in geochemical characteristics and metamorphic conditions, two possible scenarios have been suggested for the genesis of the Geita TTs (Fig. 14a and b). Each of the proposed models is in consistence with one of the abovementioned origins of the parental Kiziba basalt. In the first scenario

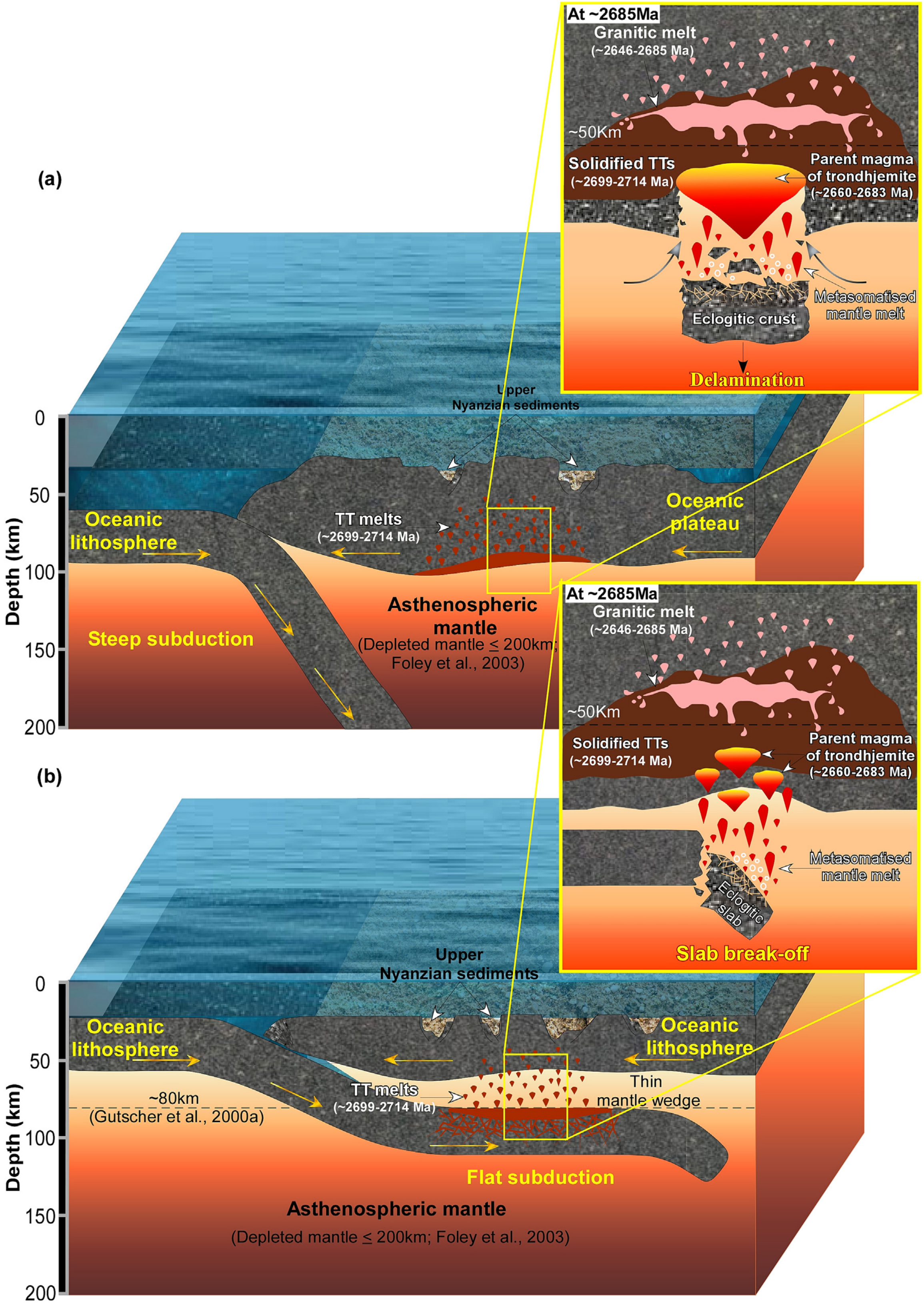

Fig. 14. Schematic models of the tectonic environment of Neoarchean Geita TTs and potassic granite illustrating two-stage partial melting mechanism. (a) Early stage (2699–2714 Ma) partial melting at the base of the oceanic basaltic plateau, generates the MP-TTs (depth ~50 km) during steep subduction. (b) Partial melting (2699–2714 Ma) during flat subduction generates the MP-TTs at a depth ~50 km. The insets in (a) and (b) show the late stage of partial melting (2646–2685 Ma) produced by the magma ascent that has been activated either by lower crustal delamination (a) or slab break-off (b). At this stage, the solidified TTs begin to produce the granitic melt at a shallower depth (<50 km). Depths for the flat slab and depleted mantle are based on Foley et al. (2003) and Gutscher et al. (2000a).

(Fig. 14a), the TTs' (2699–2714 Ma) parental melt was generated by partial melting at the base of an overriding thickened oceanic plateau that was metamorphosed at the garnet zone of the middle amphibolite facies (e.g., Smithies, 2000; Condie, 2005; Almeida et al., 2011; Wu et al., 2023). Overthickening of the anomalously thick (~50 km; Bédard et al., 2013 and reference therein) oceanic plateau by deposition of the overlying Upper Nyanzian thick pile (>2700 Ma; Sanislav et al., 2018a) enhanced partial melting (Harris and Bédard, 2014). Residual garnet and amphibole and instability of plagioclase infer that partial melting could have taken place at water-saturated metamorphic conditions (Palin et al., 2016). Partial melting is further enhanced by hydration of the root of the plateau (Kleinhanns et al., 2003; Hastie et al., 2023; and references therein) through crustal resurfacing and overturning that could have facilitated the transfer of the water into great depths. This scenario is consistent with subduction initiation stage of the model suggested by Sanislav et al. (2018a) for the northern Tanzania Craton.

In the second scenario (Fig. 14b), the TTs parental melt (2699–2714 Ma) was generated by partial melting of a 'flat' subducting slab (e.g., Smithies et al., 2003; Van Hunen et al., 2008; Ganade et al., 2017). The down going slab had a geothermal gradient high enough to motivate the melting rather than dehydrate the slab (Martin, 1999; Smithies, 2000; Martin and Moyen, 2002; Van Hunen et al., 2008; Rapp et al., 2010), (i.e. the breakdown of hydrous minerals such as amphibole, chlorite, serpentine and zoisite; Liu et al., 2020), and hence precluded metasomatism of the mantle wedge by LILE-rich fluid (e.g. Martin, 1999; Martin and Moyen, 2002; Kamber et al., 2002; Zhang et al., 2013; Liu et al., 2020). The thin mantle wedge above the low angle or 'flat' slab would have lowered the degree of mantle-melt interaction (Martin, 1999; Smithies, 2000; Martin et al., 2005).

In both scenarios, a metasomatised mantle source of the transitional granitoid (2660–2683 Ma) could be attributed to lower crust delamination/ slab break-off. Mantle upwelling accompanied the delamination process, in one hand fractionated into the transitional granitoid (2660–2683 Ma), and in the other, could have imparted the heat required to partially melt the TTs to form the potassic granite (2646–2685 Ma) at shallower crustal levels (Fig. 14 a and b; inset) (e.g., Almeida et al., 2011; Li et al., 2022). Although the two models are suitable for the Neoarchean Geita granitoids and consistent with each of suggestive Kiziba basalt origins, the high temperature (~950 °C) and low hydrous condition at which potassic granite was generated favors the first scenario (Fig. 14a).

6. Conclusion

(1) Geochemical and thermochronological data integrated with field relationships show that the Neoarchean Geita granitoids, the southern margin of the GGB, are distinguished mainly into three varieties; tonalite-trondhjemites (TTs; 2699–2714 Ma), transitional granitoid (TRANG; 2660–2683 Ma) and potassic granite (2646–2685 Ma).

(2) Residual minerals deduced from trace element modeling together with the classic Ti-in-zircon thermometery and thermodynamic modeling imply that two melting events occurred at MT/MP and HT/LP of high- and low-grade amphibolite facies, respectively. The earlier event generated the tonalitic-low silica trondhjemitic melt from Kiziba basalt, whereas the younger coincides with the generation of potassic granite that was derived from the TTs. Fractional crystallization is the most probable mechanism for high-silica trondhjemite and TRANG that were originated from tonalitic and high-K mafic magmas, respectively.

(3) Shifting from sodic to potassic magmatism, and increase in Th/Nb and Rb/Sr ratios indicate the progressive chemical maturation of an early continental crust in the Northern Tanzania Craton.

(4) Highly fractionated REE and distinctive negative Nb-Ta-Ti anomalies as well as crustal scale linear shear zone imply that the parental magmas of Neoarchean Geita granitoids might have been introduced at a convergent plate boundary.

(5) Parental melt of the older TTs could have originated at the garnet zone of the amphibolite facies by partial melting of either an overriding thickened oceanic plateau or of a flat' subducting slab. Slab break-off/lower crust delamination of the pyroxene-garnet residue might have caused mantle metasomatism responsible for the production of a metasomatised mantle melt. The produced melt could have fractionated into the younger trondhjemite phase, and heated the older TTs to generate the potassic granite melt.

CRediT authorship contribution statement

I. Gamal-Adeen: Writing – original draft, Visualization, Data curation, Formal analysis, Conceptualization. **M.G. Shahien:** Supervision. **A.M. Zayed:** Supervision. **B.R. Bakhit:** Supervision. **I. V. Sanislav:** Supervision, Resources, Methodology, Funding acquisition, Investigation, Conceptualization. **A.S.A.A. Abu Sharib:** Writing – review & editing, Supervision, Validation, Conceptualization.

Declaration of competing interest

The authors declare that they have no known competing financial interests or personal relationships that could have appeared to influence the work reported in this paper.

Acknowledgements

I. Gamal-Adeen thanks Dr. Rabea Ali, Beni-Suef University, for valuable discussion on some geochemical data during the preparation of the manuscript. The authors gratefully acknowledge the Associate Editor Federico Lucci for editorial handling. Anonymous reviewers in addition to the editor are greatly acknowledged. Their critical comments and suggestions significantly improved the manuscript.

Appendix A. Supplementary data

Supplementary data to this article can be found online at https://doi.org/10.1016/j.gsf.2026.102279.

References

Almeida, J.A.C., Dall'Agnola, R., Oliveira, M.A., Macambira, M.J.B., Pimentel, M.M., Rämö, O.T., Guimarães, F.V., Leite, A.A.S., 2011. Zircon geochronology, geochemistry and origin of the TTG suites of the Rio Maria granite-greenstone terrane: implications for the growth of the Archean crust of the Carajás provinc Brazil. Precambrian Res. 187, 201–221.

Almeida, J.A.C., Dall'Agnolam, R., Leite, A.A.S., 2013. Geochemistry and zircon geochronology of the Archean granite suites of the Rio Maria granite-greenstone terrane, Carajás Province Brazil. J. S. Am. Earth. Sci. 42, 103–126.

Anders, E., Grevesse, N., 1989. Abundances of the elements: meteoritic and solar. Geochim. Cosmochim. Acta 53 (1), 197–214.

Baker, F., 1979. Trondhjemite: Definition, environment and hypothesis of origin. In: Baker, F. (Ed.), Trondhjemites, Dacites and Related Rocks. Elsevier, Amsterdam, pp. 1–12.

Barth, H., 1990. Provisional geological map of the Lake Victoria Goldfields, Tanzania, 1:500,000 (with explanation notes). Geol. Jb. B 72, 3–59.

Bédard, J.H., 2006. A catalytic delamination-driven model for coupled genesis of Archaean crust and sub-continental lithospheric mantle. Geochim. Cosmochim. Acta 70 (5), 1188–1214.

Bédard, J.H., Harris, L.B., Thurston, P., 2013. The hunting of the snArc. Precambrian Res. 229, 20–48.

Belousova, E.A., Griffin, W.L., O'Reilly, S.Y., 2006. Zircon crystal morphology, trace element signatures and Hf isotope composition as a tool for oetrogenetic modelling: examples from Eastern Australian granitoids. J. Petrol. 47 (2), 329–353.

Blewett, R., Czarnota, K., Henson, P.A., 2010. Structural-event framework for the eastern Yilgarn Craton, Western Australia, and its implications for orogenic gold. Precambrian Res. 183 (2), 203–229.

Blichert-Toft, J., Puchtel, I.S., 2010. Depleted mantle sources through time: evidence from Lu–Hf and Sm–Nd isotope systematics of Archean komatiites. Earth Planet. Sci. Lett. 297, 598–606.

Borg, G., Shackleton, R.M., 1997. The Tanzania and NE-Zaire Cratons. In: deWit, M., Ashwal, L.D. (Eds.), Greenstone Belts. Oxford University Press, pp. 608–619.

Bao, H., Liu, S.W., Wan, Y.S., Wang, M.J., Sun, G.Z., Gao, L., Wang, W., Fu, J.H., 2022. Neoarchean granitoids and tectonic regime of lateral growth in northeastern North China Craton. Gondwana Res. 107, 176–200.

Card, K.D., 1990. A review of the superior province of the Canadian shield, a product of Archean accretion. Precambrian Res. 48, 99–156. https://doi.org/10.1016/0301-9268(90)90059-Y.

Cassidy, K.F., Champion, D.C., Krapez, B., Barley, M.E., Brown, S.J.A., Blewett, R.S., Groenewald, P.B., Tyler, I.M., 2006. A revised geological framework for the Yilgarn Craton. Geological Survey of Western Australia, Western Australia.

Castillo, P.R., 2012. Adakite petrogenesis. Lithos 134–135, 304–316.

Chadwick, B., Hedge, G.V., Allan, J.N., Vasudev, V.N., 2001. Syenite emplacement during accretion of the late Archaean Dharwar batholith, South India: SHRIMP U/Pb age and structure of the Koppal pluton Karnataka. J. Geol. Soc. India 58 (5), 381–390.

Clifford, T.N., 1970. The structural framework of Africa. In: Clifford, T.N., Gass, L.G. (Eds.), African Magmatism and Tectonics. Oliver and Boyd, Edinburgh, pp. 1–26.

Condie, K.C., 1997. Contrasting sources for upper and lower continental crust: the greenstone connection. J. Geol. 105, 729–736.

Condie, K.C., 2005. TTGs and adakites: are they both slab melts? Lithos 80 (1–4), 33–44.

Cook, Y.A., Sanislav, I.V., Hammerli, J., Blenkinsop, T.G., Dirks, P.H.G.M., 2016. A primitive mantle source for the Neoarchean mafic rocks from the Tanzania Craton. Geosci. Front. 7 (6), 911–926. https://doi.org/10.1016/j.gsf.2015.11.008.

Corfu, F., Hanchar, J.M., Hoskin, P.W.O., Kinny, P., 2003. Atlas of zircon textures. Rev. Mineral. Geochem. 53 (1), 469–500.

Czarnota, K., Champion, D.C., Goscombe, B., Blewett, R.S., Cassidy, K.F., Henson, P.A., Groenewald, P.B., 2010. Geodynamics of the eastern Yilgarn Craton. Precambrian Res. 183, 175–202. https://doi.org/10.1016/j.precamres.2010.08.004.

Dessimoz, M., Müntener, O., Ulmer, P., 2012. A case for hornblende dominated fractionation of arc magmas: the Chelan complex (Washington Cascades). Contrib. Mineral. Petrol. 163 (4), 567–589.

Drummond, M.S., Defant, M.J., 1990. A model from trondhjemite–tonalite–dacite genesis and crustal growth via slab melting: Archaean to modern comparisons. J. Geophys. Res. 95, 21503–21521.

Foley, S.F., Barth, M.G., Jenner, G.A., 2000. Rutile/melt partition coefficients for trace elements and an assessment of the influence of rutile on the trace element characteristics of subduction zone magmas. Geochim. Cosmochim. Acta 64, 933–938.

Foley, S.F., Buhre, S., Jacob, D.E., 2003. Evolution of the Archaean crust by delamination and shallow subduction. Nature 421, 249–252.

Foley, S., Tiepolo, M., Vannucci, R., 2002. Growth of early continental crust controlled by melting of amphibolite in subduction zones. Nature 417 (6891), 837–840.

Foley, S.A., 2008. Trace element perspective on Archean crust formation and on the presence or absence of Archean subduction. Spec. Pap. Geol. Soc. Am. 440, 31–50.

Frost, B.R., Barnes, C.O., Collins, W.J., Arculus, R.J., Ellis, D.J., Frost, C.D., 2001. A geochemical classification for granitic rocks. J. Petrol. 42, 2033–2048.

Gabert, G., 1990. Lithostratigraphic and tectonic setting of gold mineralization in the Archaean Cratons of Tanzania and Uganda East Africa. Precambrian Res. 46, 59–69.

Ganade, C.E., Basei, M.A.S., Grandjean, F.C., Armstrong, R., Brito, R.S., 2017. Contrasting Archaean (2.85–2.68 Ga) TTGs from the Tróia Massif (NE-Brazil) and their geodynamic implications for flat to steep subduction transition. Precambrian Res. 297, 1–18. https://doi.org/10.1016/j.precamres.2017.05.00.7.

García-Arias, M., Corretgé, L.G., Castro, A., 2012. Trace element behavior during partial melting of Iberian orthogneisses: an experimental study. Chem. Geol. 292–293, 1–17.

Green, E.C.R., White, R.W., Diener, J.F.A., Powell, R., Holland, T.J.B., Palin, R.M., 2016. Activity-composition relations for the calculation of partial melting equilibria in metabasic rocks. J. Metamorphic Geol. 34, 845–869.

Gutscher, M.-A., Maury, R., Eissen, J.-P., Bourdon, E., 2000a. Can slab melting be caused by flat subduction? Geology 28, 535–538.

Gutscher, M.-A., Spakman, W., Bijwaard, H., Engdahl, E.R., 2000b. Geodynamics of flat subduction: seismicity and tomographic constraints from the Andean margin. Tectonics 19, 814–833.

Halla, J., van Hunen, J., Heilimo, E., Hölttä, P., 2009. Geochemical and numerical constraints on Neoarchean plate tectonics. Precambrian Res. 174 (1–2), 155–162.

Halla, J., Whitehouse, M.J., Ahmad, T., Bagai, Z., 2017. Archaean granitoids: an overview and significance from a tectonic perspective. Geol. Soc. Spec. Publ. 449 (1), 1–18.

Harris, L.B., Bédard, J.H., 2014. Crustal evolution and deformation in a non-plate-tectonic archaean earth: comparisons with venus. In: Dilek, Y., Furnes, H. (Eds.), Evolution of Archean Crust and Early Life. Modern Approaches in Solid Earth Sciences. Springer, Dordrecht. https://doi.org/10.1007/978-94-007-7615-9_9.

Hastie, A.R., Law, S., Bromiley, G.D., Fitton, J.G., Harley, S.L., Muir, D.D., 2023. Deep formation of Earth's earliest continental crust consistent with subduction. Nat. Geosci. 16 (9), 816–821.

Holland, T.J.B., Powell, R., 2011. An improved and extended internally consistent thermodynamic dataset for phases of petrological interest, involving a new equation of state for solids. J. Metamorphic Geol. 29, 333–383.

Huang, H., Polat, A., Fryer, B.J., 2013. Origin of Archean tonalite – trondhjemite – granodiorite (TTG) suites and granites in the Fiskenæsset region, southern West Greenland: Implications for continental growth. Gondwana Res. 23 (2), 452–470. https://doi.org/10.1016/j.gr.2011.12.001.

Hawkesworth, C.J., Dhuime, B., Pietranik, A.B., Cawood, P.A., Kemp, A.I.S., Storey, C. D., 2010. The generation and evolution of the continental crust. J. Geol. Soc. London. 167, 229–248.

Jagoutz, O., Schmidt, M.W., Enggist, A., Burg, J.-P., Hamid, D., Hussain, S., 2013. TTG-type plutonic rocks formed in a modern arc batholith by hydrous fractionation in the lower arc crust. Contrib. Mineral Petrol. 166 (4), 1099–1118.

Jaguin, J., Gapais, D., Poujol, M., Boulvais, P., Moyen, J.-F., 2012. The Murchison greenstone belt (South Africa): a general tectonic framework. S. Afr. J. Geol. 115 (1), 65–76.

Jiang, Y.H., Ling, H.F., Jiang, S.Y., Fan, H.H., Shen, W.Z., Ni, P., 2005. Petrogenesis of a late Jurassic Peraluminous Volcanic complex and its high-Mg, potassic, quenched enclaves at Xiangshan Southeast China. J. Petrol. 46 (6), 1121–1154.

Joshi, K.B., Bhattacharjee, J., Rai, G., Halla, j., Ahmad, T., Kurhila, M.I., Choudary, A.K., 2016. The diversification of granitoids and plate tectonic implications at the Archaean–Proterozoic boundary in the Bundel khand craton, Central India. In: Halla, J., White house, M.J., Ahmad, T., Bagai, Z. (Eds.), Crust Mantle Interactions and Granitoid Diversification: Insights from Archaean Cratons. Geological Society, London, Special Publications, pp.123–157.

Kabete, J.M., McNaughton, N.J., Groves, D.I., Mruma, A.H., 2012. Reconnaissance SHRIMP U-Pb zircon geochronology of the Tanzania Craton: evidence for Neoarchean granitoid-greenstone belts in the Central Tanzania Region and the Southern East African Orogen. Precambrian Res. 216–219, 232–266. https://doi.org/10.1016/j.precamres.2012.06.020.

Kamber, B.S., Ewart, A., Collerson, K.D., Bruce, M.C., McDonald, G.D., 2002. Fluid-mobile trace element constraints on the role of slab melting and implications for Archaean crustal growth models. Contrib. Mineral. Petrol. 144 (1), 38–56.

Keller, C.B., Schoene, B., 2012. Statistical geochemistry reveals disruption in secular lithospheric evolution about 2.5 Gyr ago. Nature 485, 490–495.

Kleinhanns, I.C., Kramers, J.D., Kamber, B.S., 2003. Importance of water for Archaean granitoid petrology: a comparative study of TTG and potassic granitoids from Barberton Mountain Land South Africa. Contrib. Mineral. Petrol. 145 (3), 377–389.

Kwelwa, S.D., Sanislav, I.V., Dirks, P.H.G.M., Blenkinsop, T., Kolling, S.L., 2018a. The petrogenesis of the Neoarchean Kukuluma Intrusive complex NW Tanzania. Precambrian Res. 305, 64–78. https://doi.org/10.1016/j.precamres.2017.12.021.

Kwelwa, S.D., Sanislav, I.V., Dirks, P., Blenkinsop, T., Kolling, S.L., 2018b. Zircon U-Pb ages and Hf isotope data from the Kukuluma Terrain of the Geita Greenstone Belt, Tanzania Craton: implications for stratigraphy, crustal growth and timing of gold mineralization. J. Afr. Earth Sci. 139, 38–54.

Laurent, O., Martin, H., Moyen, J.F., Doucelance, R., 2014. The diversity and evolution of late-Archean granitoids: evidence for the onset of "modern-style" plate tectonics between 3.0 and 2.5 Ga. Lithos 205, 208–235. https://doi.org/10.1016/j.lithos.2014.06.012.

Li, S., Li, X., Zhou, J., Cao, H., Liu, L., Liu, Y., Sun, G., Suo, Y., Li, Y., Yu, S., Jiang, Z., 2022. Passive magmatism on Earth and Earth-like planets. Geosyst. Geoenviron. 1 (1), 100008.

Liou, P., Guo, J., 2019. Generation of archaean TTG gneisses through amphibole-dominated fractionation. J. Geophys. Res. Solid Earth. 124 (4), 3605–3619.

Liu, H., Sun, W.-D., Deng, J.-H., 2020. Transition of subduction-related magmatism from slab melting to dehydration at 2.5 Ga. Precambrian Res. 337, 105524. https://doi.org/10.1016/j.precamres.2019.105524.

Liu, S., Bao, H., Sun, G., Wang, W., Fu, J., Gao, L., Guo, R., Hu, Y., 2022. Archean crust-mantle geodynamic regimes: a review. Geosyst. Geoenviron. 1 (3), 100063.

Liu, H., Wang, Y., Deng, J., Zhang, Y., Chen, Q., Liao, R., Sun, W., 2023. Modern-style arc magmatism since ca. 2.2 billion years ago revealed by Nb/Ta-Dy/Yb systematics in igneous rocks. Chem. Geol. 638, 121710.

Maboko, M., Pedersen, R., Manya, S., Torssander, P., Mwache, M., 2006. The origin of late archaean granitoids in the Sukumaland greenstone belt of Northern Tanzania: geochemical and isotopic constraints Tanzania. J. Sci. 32 (1).

Manikyamba, C., Kerrich, R., 2012. Eastern Dharwar Craton, India: continental lithosphere growth by accretion of diverse plume and arc terranes. Geosci. Front. 3, 225–240. https://doi.org/10.1016/j.gsf.2011.11.009.

Manya, S., Maboko, M.A.H., 2003. Dating basaltic volcanism in the Neoarchaean Sukumaland Greenstone Belt of the Tanzania Craton using the Sm–Nd method: implications for the geological evolution of the Tanzania Craton. Precambrian Res. 121, 35–45.

Manya, S., Makenya, A.H., Maboko, E.N., 2007. Geochemistry and Nd-isotopic composition of potassic magmatism in the Neoarchaean Musoma-Mara Greenstone Belt, northern Tanzania. Precambrian Res. 159, 231–240.

Manya, S., Maboko, M.A.H., 2008. Geochemistry of the Neoarchaean mafic volcanic rocks of the Geita area, NW Tanzania: implications for stratigraphical relationships in the Sukumaland greenstone belt. J. Afr. Earth Sci. 52, 152–160.

Manya, S., 2016. Petrogenesis and emplacement of the TTG and K-rich granites at the Buzwagi gold mine, northern Tanzania: implications for the timing of gold mineralization. Lithos 256–257, 26–40. https://doi.org/10.1016/j.lithos.2016.03.025.

Marimon, R.S., Hawkesworth, C.J., Dantas, E.L., Trouw, R.A.J., Teixeira, W., Hackspacher, P.C., Fetter, A., Ávila, C.A., Volante, S., Corrêa Neto, A.V., Bongiolo, E.M., Vinagre, R., Simon, M., et al., 2022. The generation and evolution of the Archean continental crust: the granitoid story in southeastern Brazil. Geosci. Front. 13 (4), 101402. https://doi.org/10.1016/j.gsf.2022.101402.

Martin, H., 1986. Effect of steeper Archean geothermal gradient on geochemistry of subduction-zone magmas. Geology 14, 753–756.

Martin, H., 1987. Petrogenesis of Archaean trondhjemites, tonalites and granodiorites from eastern Finland: major and trace element geochemistry. J. Petrol. 28, 921–953.

Martin, H., 1999. Adakitic magmas: modern analogues of Archaean granitoids. Lithos 46 (3), 411–429.

Martin, H., Moyen, J.F., 2002. Secular changes in tonalite-trondhjemite-granodiorite composition as markers of the progressive cooling of Earth. Geology 30 (4), 319–322.

Martin, E., Sigmarsson, O., 2005. Trondhjemitic and granitic melts formed by fractional crystallization of an olivine tholeiite from Reykjanes Peninsula Iceland. Geol. Mag. 142 (6), 651–658.

Martin, H., Smithies, R.H., Rapp, R., Moyen, J.F., Champion, D., 2005. An overview of adakite, tonalite-trondhjemiten-granodiorite (TTG), and sanukitoid: relationships and some implications for crustal evolution. Lithos 79 (1–2), 1–24.

Martin, E., Sigmarsson, O., 2010. Thirteen million years of silicic magma production in Iceland: Links between petrogenesis and tectonic settings. Lithos 116 (1–2), 129–144. https://doi.org/10.1016/j.lithos.2010.01.005.

Martin, H., Moyen, J.-F., Guitreau, M., Blichert-Toft, J., Le Pennec, J.-L., 2014. Why Archaean TTG cannot be generated by MORB melting in subduction zones. Lithos 198–199 (1), 1–13. https://doi.org/10.1016/j.lithos.2014.02.017.

Messo, C., Manya, S., Maboko, M.A.H., 2012. Geochemistry of the Neoarchaean volcanic rocks of the Kilimafedha greenstone belt, Northeastern Tanzania. J. Geol. Res. 2012, 603971.

Moyen, J.-F., Martin, H., Jayananda, M., Auvray, B., 2003. Late Archaean granites: a typology based on the Dharwar Craton (India). Precambrian Res. 127, 103–123.

Moyen, J.F., Stevens, G., 2006. Experimental constraints on TTG petrogenesis: Implications for archean geodynamics. Geophys. Monogr. Ser. 164, 149–175.

Moyen, J.F., Stevens, G., Kisters, A.F.M., Belcher, R.W., 2007. TTG plutons of the barberton granitoid-greenstone Terrain, South Africa. In: Van Kranendonk, J.M., Smithies, R.H., Bennett V.C. (Eds.), Earth's Oldest Rocks. Dev. Precambrian Geol. 15(07), 607–667.

Middlemost, E.A.K., 1985. Naming materials in the magma/igneous rock system. Earth-Sci. Rev. 37, 215–224.

Moyen, J.F., 2011. The composite Archaean grey gneisses: petrological significance, and evidence for a non-unique tectonic setting for Archaean crustal growth. Lithos 123 (1–4), 21–36. https://doi.org/10.1016/j.lithos.2010.09.015.

Moyen, J.F., Laurent, O., 2018. Archaean tectonic systems: a view from igneous rocks. Lithos 302–303, 99–125. https://doi.org/10.1016/j.lithos.2017.11.038.

Moyen, J.F., Martin, H., 2012. Forty years of TTG research. Lithos 148, 312–336. https://doi.org/10.1016/j.lithos.2012.06.010.

Mshiu, E.E., Maboko, M.A.H., 2012. Geochemistry and petrogenesis of the late Archaean high-K granites in the southern Musoma-Mara Greenstone Belt: their influence in evolution of Archaean Tanzania Craton. J. Afr. Earth Sci. 66–67, 1–12. https://doi.org/10.1016/j.jafrearsci.2012.03.002.

Mtoro, M., Maboko, M.A.H., Manya, S., 2009. Geochemistry and geochronology of the bimodal volcanic rocks of the Suguti area in the southern part of the Musoma-Mara Greenstone Belt NorthernTanzania. Precambrian Res. 174, 241–257.

Nair, R., Chacko, T., 2008. Role of oceanic plateaus in the initiation of subduction and origin of continental crust. Geology 36, 583–586.

O'Connor, J.T., 1965. A classification for quartz-rich igneous rocks based on feldspar ratios. U.S. Geological Survey Professional Paper 525, 79–84.

Olierook, H.K.H., Barham, M., Kirkland, C.L., Hollis, J., Vass, A., 2020. Zircon fingerprint of the Neoproterozoic North Atlantic: perspectives from East Greenland. Precambrian Res. 342, 105653. https://doi.org/10.1016/j.precamres.2020.105653.

Palin, R.M., White, R.W., Green, E.C.R., 2016. Partial melting of metabasic rocks and the generation of tonalitic–trondhjemitic–granodioritic (TTG) crust in the Archaean: constraints from phase equilibrium modelling. Precambrian Res. 287, 73–90. https://doi.org/10.1016/j.precamres.2016.11.001.

Pearce, J.A., Harris, N.B.W., Tindle, A.G., 1984. Trace elements discrimination diagrams for the tectonic interpretation of granitic rocks. J. Petrol. 25, 956–983.

Peck, W.H., Valley, J.W., Wilde, S.A., Graham, C.M., 2001. Oxygen isotope ratios and rare earth elements in 3.3 to 4.4 Ga zircons: ion microprobe evidence for high δ^{18}O continental crust and oceans in the Early Archean. Geochim. Cosmochim. Acta 65, 4215–4229.

Percival, J.A., Sanborn-Barrie, M., Skulski, T., Stott, G.M., Helmstaedt, H., White, D.J., 2006. Tectonic evolution of the western Superior Province from NATMAP and Lithoprobe studies. Can. J. Earth Sci. 43, 1085–1117.

Polat, A., Kerrich, R., Wyman, D.A., 1998. The late Archean Schreiber–Hemlo and White River–Dayohessarah greenstone belts, Superior Province: collages of oceanic plateaus, oceanic arcs, and subduction–accretion complexes. Tectonophysics 289, 295–326. https://doi.org/10.1016/S0040-1951(98)00002-X.

Prouteau, G., Scaillet, B., Pichavant, M., Maury, R., 2001. Evidence for mantle metasomatism by hydrous silicic melts derived from subducted oceanic crust. Nature 410 (6825), 197–200.

Rapp, P.R., 1997. Heterogeneous source regions for Archean granitoids: Experimental and geochemical evidence. In: de Wit, M.J., Ashwal, L.D. (Eds.), Greenstone Belts. Oxford University Press, Oxford.

Rapp, R.P., Shimizu, N., Norman, M.D., 2003. Growth of early continental crust by partial melting of eclogite. Nature 425 (6958), 605–609.

Rapp, R.P., Norman, M.D., Laporte, D., Yaxley, G.M., Martin, H., Foley, S.F., 2010. Continent formation in the Archean and chemical evolution of the cratonic lithosphere: Melt-rock reaction experiments at 3-4 GPa and petrogenesis of Archean Mg-diorites (Sanukitoids). J. Petrol. 51, 1237–1266.

Roberts, N.M.W., Van Kranendonk, M.J., Parman, S., Clift, P.D., 2015. Continent formation through time. In: Roberts, N.M.W., Van Kranendonk, M.J., Parman, S., Shirey, S., Clift, P.D. (Eds.), Continent Formation Through Time. J. Geol. Soc. London, Special Publications, 389, pp. 1–16.

Rollinson, H.R., 1993. Using Geochemical Data: Evolution, Presentation, Interpretation. Longman Scientific & Technical.

Rollinson, H.R., Pease, V., 2021. Using Geochemical Data to Understand Geological Processes. Cambridge University Press.

Rubatto, D., 2002. Zircon trace element geochemistry: partitioning with garnet and the link between U-Pb ages and metamorphism. Chem. Geol. 184 (1–2), 123–138.

Rudnick, R.L., Gao, S., 2014. Composition of the Continental Crust. In: Holland, H.D., Turekian, K.K. (Eds.), Treatise on Geochemistry, second ed. Elsevier, pp. 1–64. http://dx.doi.org/10.1016/B978-0-08-095975-7.00301-6.

Saki, A., Lucci, F., Miri, M., White, J.C., 2021. Trondhjemite leucosomes generated by partial melting of a hornblende-gabbro (Alvand plutonic complex, Hamedan, NW Iran). Int. Geol. Rev. 64 (5), 597–630.

Sanislav, I.V., Wormald, R.J., Dirks, P.H.G.M., Blenkinsop, T.G., Salamba, L., Joseph, D., 2014. Zircon U-Pb ages and Lu-Hf isotope systematics from late-tectonic granites, Geita Greenstone Belt: implications for crustal growth of the Tanzania Craton. Precambrian Res. 242, 187–204. https://doi.org/10.1016/j.precamres.2013.12.026.

Sanislav, I.V., Kolling, S.L., Brayshaw, M., Cook, Y.A., Dirks, P.H.G.M., Blenkinsop, T.G., Mturi, M.I., Ruhega, R., 2015. The geology of the giant Nyankanga gold deposit, Geita Greenstone Belt Tanzania. Ore Geol. Rev. 69, 1–16.

Sanislav, I.V., Blenkinsop, T.G., Dirks, P.H.G.M., 2018a. Archaean crustal growth through successive partial melting events in an oceanic plateau-like setting in the Tanzania Craton. Terra Nov. 30 (3), 169–178.

Sanislav, I.V., Dirks, P.H.G.M., Blenkinsop, T., Kolling, S.L., 2018b. The tectonic history of a crustal-scale shear zone in the Tanzania Craton from the Geita Greenstone Belt NW-Tanzania Craton. Precambrian Res. 310, 1–16. https://doi.org/10.1016/j.precamres.2018.02.025.

Sisson, T.W., Ratajeski, K., Hankins, W.B., Glazner, A.F., 2005. Voluminous granitic magmas from common basaltic sources. Contrib. Mineral. Petrol. 148 (6), 635–661.

Smithies, R.H., 2000. The Archaean tonalite-trondhjemite-granodiorite (TTG) series is not an analogue of Cenozoic adakite. Earth Planet. Sci. Lett. 182 (1), 115–125.

Smithies, R.H., Champion, D.C., Cassidy, K.F., 2003. Formation of Earth's early Archaean continental crust. Precambrian Res. 127 (1–3), 89–101.

Smithies, R.H., Champion, D.C., Van Kranendonk, M.J., 2009. Formation of Paleoarchean continental crust through infracrustal melting of enriched basalt. Earth Planet. Sci. Lett. 281 (3–4), 298–306. https://doi.org/10.1016/j.epsl.2009.03.003.

Smithies, R.H., Lu, Y., Johnson, T.E., Kirkland, C.L., Cassidy, K.F., Champion, D.C., Mole, D.R., Zibra, I., Gessner, K., Kirkland, C.L., Cassidy, K.F., Sapkota, J., De Paoli, M.C., Poujol, M., 2019. No evidence for high-pressure melting of Earth's crust in the Archean. Nat. Commun. 10 (1), 1–12. https://doi.org/10.1038/s41467-019-13547-x.

Sun, G., Liu, S., Wang, M., Bao, H., Ten, G., 2020. Complex Neoarchean mantle metasomatism: Evidence from sanukitoid diorites-monzodiorites-granodiorites in the northeastern North China Craton. Precambrian Res. 342, 105692.

Sun, S.S., McDonough, W.F., 1989. Chemical and isotopic systematics of oceanic basalts: implications for mantle composition and processes. Geol. Soc. Spec. Publ. 42 (1), 313–345.

Sun, G.Z., Liu, S.W., Li, S.Z., Bao, H., Wang, W., Guo, R.R., Fu, J.H., Gao, L., Hu, Y.L., Wang, X., Yu, S.Y., Dai, L.M., 2024. Neoarchean granitoid magmatism and geodynamic process in the northeastern North China Craton. Geol. Soc. Am. Bull. 136 (11–12), 5091–5108.

Sun, G.Z., Liu, S.W., Cawood, P.A., Tang, M., van Hunen, J., Gao, L., Hu, Y.L., Hu, F.Y., 2021. Thermal state and evolving geodynamic regimes of the Meso- to Neoarchean North China Craton. Nat. Commun. 12, 3888.

Sun, G.Z., Liu, S.W., Li, S.Z., Kusky, T.M., Hu, F.Y., Bao, H., Gao, L., Hu, Y.L., Yu, S.Y., Dai, L.M., Wang, L.T., Wang, X., 2025. Neoarchean orogenic belt evolution in the northeast North China Craton: implications for the reconstruction of early Earth's microplates. Precambrian Res. 417, 107659.

Tsay, A., Zajacz, Z., Sanchez-Valle, C., 2014. Efficient mobilization and fractionation of rare-earth elements by aqueous fluids upon slab dehydration. Earth Planet. Sci. Lett. 398, 101–112. https://doi.org/10.1016/j.epsl.2014.04.042.

Ustunisik, G., Kilinc, A., 2011. The role of fractional crystallization, magma recharge, and magma mixing in the differentiation of the Small Hasandag volcano, Central Anatolia Turkey. Lithos 125 (3–4), 984–993. https://doi.org/10.1016/j.lithos.2011.05.013.

Van Hunen, J., Van Keken, P.E., Hynes, A., Davies, G.F., 2008. Tectonics of early Earth: Some geodynamic considerations. Geol. Soc. Am. Spec. Pap. 440, 157–171.

Watson, E.B., Wark, D.A., Thomas, J.B., 2006. Crystallization thermometers for zircon and rutile. Contrib. Mineral. Petrol. 151, 413–433. https://doi.org/10.1007/s00410-006-0068-5.

Weinberg, R., Hasalová, P., 2015. Water-fluxed melting of the continental crust: a review. Lithos 212, 158–188.

Whalen, J.B., Percival, J.A., McNicoll, V.J., Longstaffe, F.J., 2002. A mainly crustal origin for tonalitic granitoid rocks, Superior Province, Canada: Implications for late Archean tectonomagmatic processes. J. Petrol. 43 (8), 1551–1570.

White, R.W., Powell, R., Holland, T.J.B., Johnson, T.E., Green, E.C.R., 2014. New mineral activity–composition relations for thermodynamic calculations in metapelitic systems. J. Metamorphic Geol. 32, 261–286.

Whitney, D., Evan, B., 2010. Abbreviations for names of rock forming minerals. Am. Mineral. 95, 185–187.

Wu, Y.B., Gao, S., Gong, H.J., Xiang, H., Jiao, W.F., Yang, S.H., Liu, Y.S., Yuan, H.L., 2009. Zircon U–Pb age, trace element and Hf isotope composition of Kongling terrane in the Yangtze Craton: refining the timing of Palaeoproterozoic high-grade metamorphism. J. Metamorphic Geol. 27, 461–477. https://doi.org/10.1111/j.1525-1314.2009.00826.x.

Wu, X., Liu, X., Sun, K., Xu, K., Sun, H., Gong, P., He, S., Machumu, G., 2023. Petrogenesis and tectonic setting of TTG rocks from the Katoro area, Sukumaland Greenstone Belt, NW Tanzania: Evidence from zircon U-Pb geochronology, Lu-Hf isotopes, whole-rock geochemistry, and Sr-Nd isotopes. Precambrian Res. 385, 106943. https://doi.org/10.1016/j.precamres.2022.106943.

Zhang, C., Holtz, F., Koepke, J., Wolff, P.E., Ma, C., Bédard, J.H., 2013. Constraints from experimental melting of amphibolite on the depth of formation of garnet-rich restites, and implications for models of Early Archean crustal growth. Precambrian Res. 231, 206–217.